Corrosion of Various Engineering Alloys in Supercritical Carbon Dioxide

by

Jonathan Paul Gibbs

B.S Marine Engineering Systems
United States Merchant Marine Academy, 2005

S.M. Nuclear Science and Engineering
Massachusetts Institute of Technology, 2008

SUBMITTED TO THE DEPARTMENT OF MATERIAL SCIENCE AND ENGINEERING IN PARTIAL FULFILLMENT OF THE REQUIREMENTS FOR THE DEGREE OF

MASTER OF SCIENCE IN MATERIALS SCIENCE AND ENGINEERING
AT THE
MASSACHUSETTS INSTITUTE OF TECHNOLGOY

June 2010

Signature of Author:_____
Department of Materials Science and Engineering
May 21, 2010

Certified by:_____
Ronald Ballinger – Thesis Supervisor
Professor of Materials Science and Engineering

Certified by:_____
Thomas McKrell – Thesis Supervisor
Research Scientist, Department of Nuclear Science and Engineering

Accepted by:_____
Christine Ortiz
Chairman, Department Committee on Graduate Students

This work is dedicated to Josiah Willard Gibbs
Thanks for being an awesome ancestor!

This page was intentionally left blank

Corrosion of Various Engineering Alloys in Supercritical Carbon Dioxide

by

Jonathan P. Gibbs

Submitted to the Department of Materials Science & Engineering on May 21, 2010 in Partial Fulfillment of the Requirements for the Degree of Master of Science in Materials Science and Engineering

Abstract

The corrosion resistance of ten engineering alloys were tested in a supercritical carbon dioxide (S-CO_2) environment for up to 3000 hours at 610°C and 20MPa. The purpose of this work was to evaluate each alloy as a potential candidate for use in the S-CO_2 cooled next generation nuclear reactors. The alloys that performed well in these tests will undergo further testing and those that performed poorly will be disqualified from future deployment in S-CO_2 applications. The ten alloys tested in this work were classified into four categories: Ferritic-martenitic steels, austenitic stainless steels, nickel alloys, and special materials. The majority of the alloys were focused on the five alloys within the austenitic stainless steel series, followed by three nickel alloys. These alloys were F91, HCM12A, 316SS, 310SS, AL-6XN, 800H, Haynes 230, Alloy 625, PE-16, and PM2000.

The experimental procedure consisted of placing multiple samples of each alloy in an autoclave and exposing them to S-CO_2 for up to 3000 hours, in 500 hour increments. At every 500 hour increment each alloy was removed from the autoclave, photo documented and weighed. One sample from each 500 hour test was reserved for future analysis while the other samples were returned to the autoclave for further testing. The 3000 hour samples were sectioned, mounted in epoxy, and polished oriented normal to its oxide growth to document the thickness and structure of each oxide layer formed.

Alloys F91 and HCM12A performed poorly and experienced substantial weight gain. Each of these alloys formed a duplex oxide layer with the outside layer being iron rich and chromium depleted and the inside layer being iron depleted and chromium rich. The oxide layers were porous and were susceptible to spallation. The 3000 hour weight gain for both of these alloys was approximately $5x10^{-3}$ mg/cm^2, which was two orders of magnitude higher than the remaining eight alloys. Alloys PM2000, 316SS, 310SS, AL-6XN, 800H, Haynes 230, Alloy 625, and PE-16 were stable oxide formers with thin, dense oxide layers and were resistant to corrosion. The weight gain of these eight alloys was on the order of $4x10^{-5}$ mg/cm^2 at 3000 hours of exposure. Overall, the alloys with high chromium and nickel contents performed the best, followed by the stainless steels with intermediate chromium content.

Thesis Supervisor: Ronald Ballinger, Ph.D.
Title: Professor, Nuclear Science and Engineering, Materials Science and Engineering

Thesis Reader: Thomas McKrell, Ph.D.
Title: Research Scientist, Nuclear Science and Engineering

This page was intentionally left blank

Acknowledgements

First and foremost, I would like to express my deepest gratitude to my two advisors: Professor Ronald Ballinger and Dr. Thomas McKrell. Professor Ballinger's expertise in materials science and engineering, careful scrutiny of my technical work, and patience have been instrumental to my success at MIT. Dr. McKrell's vast, practical knowledge in the field of material science and expertise in experimental work have helped me immensely.

I would also like to thank Gary Eastwick for his valuable and unselfish work in getting me acclimated with the S-CO_2 corrosion experiment.

Finally, I would like to thank the exceptional people at Sandia National Laboratory, Los Alamos National Laboratory, and Lockheed Martin for their generous support on the supercritical carbon dioxide work. Their alloy contributions and financial support made this work possible.

Table of Contents

List of Figures

List of Tables

This page was intentionally left blank

Chapter 1 - Introduction and Overview

1.1 Introduction

As the global energy demand continues to increase the demand for energy resources becomes more competitive. This is further exacerbated by the demand for low-carbon energy. Ultimately nuclear is the most viable option for large scale, clean energy production. Currently, nuclear energy accounts for about 15% of the world's energy supply[1] and 20% in the United States.[2] The Generation-IV nuclear reactor designs are designed to increase the safety margins, efficiency, and reduce overall costs and in some cases provide for waste reduction through actinide burning. The supercritical carbon dioxide (S-CO_2) cooled nuclear reactor is one of the six Gen-IV nuclear reactor designs currently under consideration for future deployment. The S-CO_2 cooled reactor is able to obtain the same plant efficiency as the helium-cooled, pebble bed reactor with a 300°C lower peak temperature (550°C vs. 850°C), but higher pressure (20 MPa vs. 8 MPa). The S-CO_2 cycles take advantage of the non-ideal properties of CO_2 near its critical point (31.1 °C and 7.38 MPa), most importantly its high density (low compressibility). This allows the compressor work fraction to be smaller than typical Brayton cycles, thus enabling achievement of higher thermodynamic efficiency at lower temperatures. Furthermore, the S-CO_2 cycle is able to achieve a modular plant design with high power density, thus, in principal, reducing the overall cost and facilitating maintenance.[3]

Carbon dioxide has been used as a primary coolant for many years in nuclear power plants. As early as the 1960s it was being used to cool the Magnox and later the advanced gas-cooled reactors (AGR) in the United Kingdom. However, little material performance data exists for materials in the S-CO_2 environments at the proposed operating conditions of the Gen-IV nuclear reactors.[4,5] These ambitious nuclear reactor designs have immense potential for improved economics, safety, and reliability, but also push the limits of the current available materials. These materials hurdles need to be overcome before any these new power plants are constructed. The work presented in this thesis is a step in the direction of qualifying materials for the next generation nuclear power plants. The corrosion testing in this work was conducted at 610 °C and 20 MPa,

which are the proposed operating conditions for the S-CO_2 cooled Gen-IV nuclear reactor.

1.2 Objectives and Contributions of this Work

The contributions and motivation for this work are to further classify and explore the suitability of various engineering alloys for deployment in S-CO_2 cooled nuclear reactors. The focus of this work is a scoping study to determine the potential alloys for further evaluation and testing. Contributions to the S-CO_2 project were testing the batches of alloy specimens from 1500-3000 hours in the S-CO_2 environment, weight gain analysis on those same batches of alloy specimens, photo documentation, and SEM surface characterization and cross-sectional oxide characterization of all specimens,

1.3 Background and History

The history of steel oxidation in CO_2 environments is well documented and understood for a wide temperature range, but limited pressure range. Accordingly, there is a scarcity of material performance data for CO_2 environments in the temperature and pressure range of interest for the S-CO_2 cooled nuclear reactors. The effect of pressure on the corrosion characteristics of engineering alloys is currently unknown. The known-to-date corrosion effects to date of CO_2 are outlined here.

The largest compilation of data is from the CO_2 cooled advanced gas reactors (AGR) which were operated for more than 40 years in the United Kingdom. The AGR experience provides corrosion data for operation times closing in on 100,000 hours for the temperature of interest (650°C), but only at 4 MPa. The proposed S-CO_2 cooled nuclear reactor has an upper operating window of 550-650°C and 20 MPa. Furthermore, the data obtained from the AGR experience is not wholly applicable because it focused on mild and low alloy steels. The high temperature and pressure combination for the S-CO_2 cycles will prohibit the use of mild and low alloy steels in the high temperature/pressure regions because they will not be able to meet code mandated strength requirements. Furthermore, very little data has been reported for oxide dispersion steel (ODS) and high alloyed ferritic steels.

The effects of high pressure on the corrosion characteristics of engineering alloys are currently unknown; thus, it is necessary to conduct various experiments to further classify acceptable materials and understand their corrosion behavior. The S-CO_2 testing is ongoing and previously published results have presented corrosion characteristics for several metallic alloys at 650°C and 12 MPa for intervals up to 3000 hours.[6] The results from the 650°C, 12 MPa, 3000 hour tests investigated the following alloys: Stainless steel 316 L; ODS steels MA956, MA957, and PM2000; and martensitic alloys HT9, T91, and the Russian alloy EP823. The alloys chosen for this work were based on the published results from the 12 MPa testing. Those alloys that performed poorly were rejected and additional alloys were added for suitability scoping.

Considerable research has been conducted on ferritic and austenitic steel alloys, albeit, as mentioned before, at lower pressures. The previous S-CO_2 corrosion work at 650 °C has been limited to approximately 12.5 MPa and has largely been focused on stainless steels. Recent corrosion work has focused on even higher temperature testing (750 °C) with primarily Ni-base superalloys, but, fortunately, included Alloy 316L for comparative purposes.[7] The materials covered in this work are focused on a mix of stainless steels, several nickel-based alloys, and also special steels, namely oxide dispersion steel. The test procedures for previous work is very similar to that outlined here.

1.4 Oxidation Overview

This section discusses oxidation principles and a brief literature review of oxidation for the generalized types of metals covered in this work.

The focus of this work is an investigation of the effects of S-CO_2 on the corrosion behavior of various alloys. The conditions of this test environment were tightly controlled to prevent ingress of other contaminants and allow for a more fundamental understanding of the corrosion effects of CO_2 on the various alloys. Using an Ellingham Diagram, it is thermodynamically possible to predict the corrosion processes (the stable

oxide phases) ongoing at a particular test condition. This diagram relates the change in Gibbs Free Energy as a function of temperature, carbon monoxide, carbon dioxide, and oxygen concentrations for reactions between a metal and the gaseous environment. It is important to note here that the Ellingham Diagram is only focused on thermodynamic possibility of a reaction, not the kinetics. Thus, a reaction may be thermodynamically favorable, but may not occur if kinetics are unachievable. The Gibbs Free Energy is a chemical potential for a reaction and is a convenient metric for expressing the spontaneity of a reaction. A negative free energy indicates that a reaction may occur spontaneously as it is thermodynamically favorable and a positive value indicates and endothermic reaction and that some additional energy needs to be applied for the reaction to proceed. Such is the case for certain types of oxidation reactions in the S-CO_2 environment. These oxidation reactions are dependent upon the partial pressure of oxygen or, in this work, also carbon monoxide and carbon dioxide. The Ellingham Diagram is used to determine the oxygen or carbon monoxide/dioxide concentration for redox reactions. Metal reduction occurs when the concentration of oxygen or carbon monoxide is below the equilibrium concentration for the reaction in question. Similarly, a metal is oxidized if the oxygen or carbon monoxide/dioxide concentration is above the equilibrium concentration.

Ideally, a desirable metal is one that forms a stable, dense, protective oxide, which prevents further base metal loss. An unstable oxide can lead to spallation, thus, loss of a protective oxide and increased metal loss. Moreover, a low-density/porous oxide can result in increased metal loss due to oxygen ion diffusion into and metal ion diffusion out of the oxide. For redox reactions in CO_2 environments, oxide stability decreases with an increase in partial pressure of oxygen and/or carbon monoxide and temperature. An Ellingham Diagram is provided in Figure 1.1 with pertinent reactions for this work highlighted.

The Ellingham Diagram has three main uses:

1. Determination of the potential of oxidizing a metal to its oxide.
2. Determination of the oxygen equilibrium partial pressure with a metal.

3. Determination of the ratio of carbon monoxide to carbon dioxide necessary to reduce metal oxide, or inversely to form an oxide.

Other important features to the Ellingham Diagram:

- Free energy of formation for most metals' redox reactions is negative. Thus, $\Delta G=0$ is at the top of the diagram. Thus, reactions lower on the graph are more thermodynamically stable.
- The diagram shown is strictly for metals forming/dissolving oxides. Similar diagrams can be construction for other reactions
- Most of the reaction lines have a positive slope: This indicates both the metal and oxide are present as condensed phases.

One notable exception to the positive trend lines is the reaction in Equation 1.1 of carbon and oxygen to form carbon monoxide:

$$2C + O_2 \Rightarrow 2CO \qquad \text{(Eq.1.1)}$$

This is a downward sloping line because there two moles of carbon (solid) reacting with one mole of oxygen (gas), leading to an increase in entropy. Thus, carbon monoxide is an effective reducing agent. This leads to oxide stability reduction with increasing temperature (i.e. for the same O_2 and CO concentration/pressure, oxide formation is less likely to occur). The reactions pertinent to the alloys in this work are circled in Figure 1.1, and include iron, nickel, chromium, aluminum, silicon, and carbon and oxygen reacting to form carbon monoxide and dioxide.

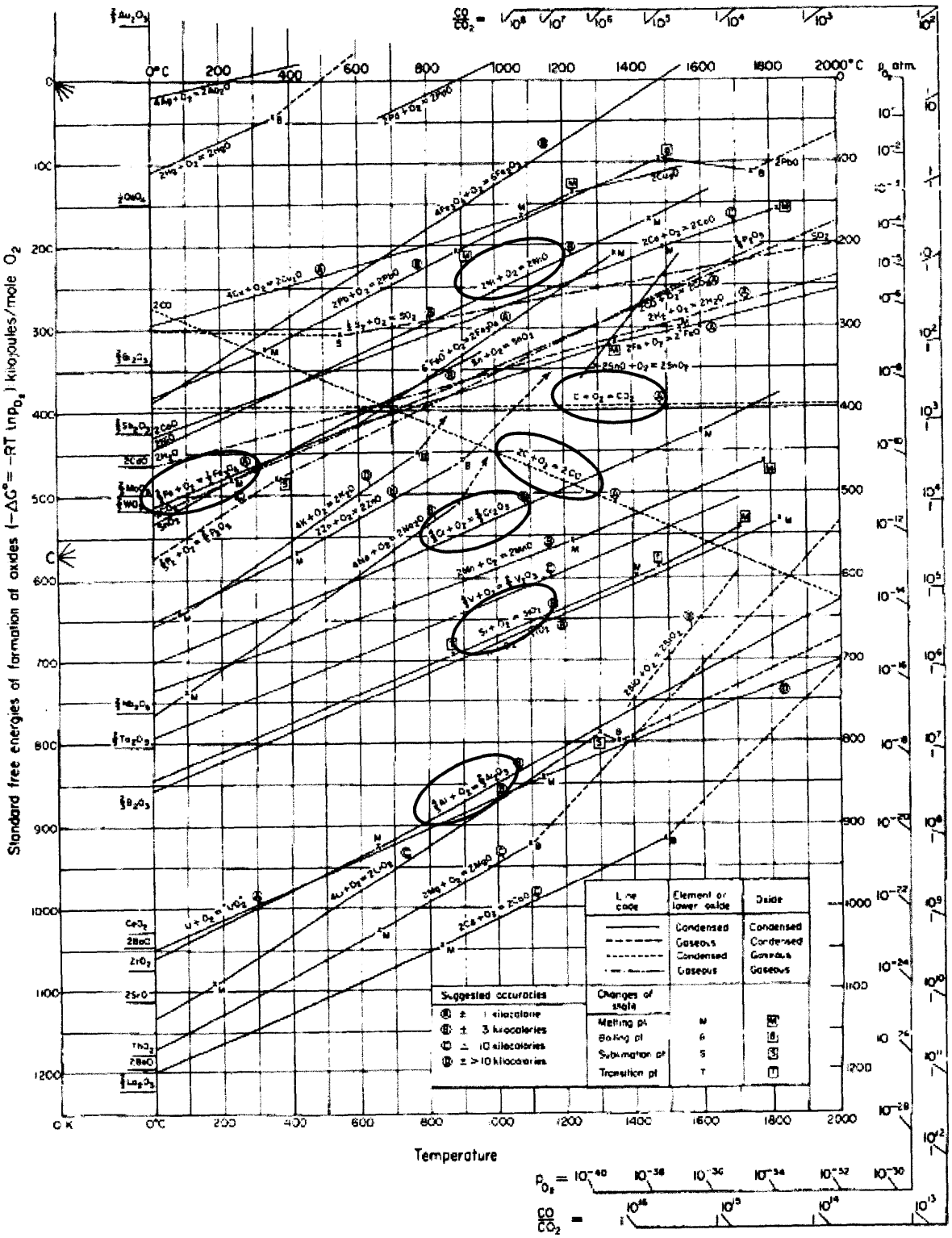

Figure 1.1: Ellingham Diagrams[8]

1.4.1 High Temperature Oxidation

In order for high temperature metal oxidation to occur, transport of metal from the metal phase to the oxide/oxygen interface, or oxygen to the metal/oxide interface, or both, must occur. The oxygen interface can be any oxidizing interface, but is referred to as the "oxygen interface" for simplicity. In the case of metal cation transport, the new oxide forms at the oxide/oxygen interface. In the case of oxygen anion transport, the oxide forms at the metal/oxide interface. When transport of both the metal cations and oxygen anions occurs the new oxide can form within itself. Thus, oxidation must occur by means of the movement of metal cations or oxygen anions (or, more generally, any oxidizing species) through an oxide phase. The metal and oxygen bonding has a characteristic mixture of ionic and covalent character; however, to a first order approximation, both the metal and oxygen may be regarded as existing ions. For the discussion here, the metal cations are represented as M^{2+}. The transport of oxygen and metal ions is depicted in Figure 1.2. Oxidation of metal consists of several steps:[9]

1. Transport of metal to the metal/oxide interface or oxygen to the oxide/oxygen interface.
2. Ionization of the metal or oxygen at the respective interface
3. Diffusion of cation, M^{2+}, or anion, O^{2-} through the oxide film
4. Oxidation of metal at the metal/oxide interface followed by reaction with the diffusing anions to form oxide. Or, reduction of oxygen at the oxide/oxygen interface followed by reaction with diffusing cations to form oxide.

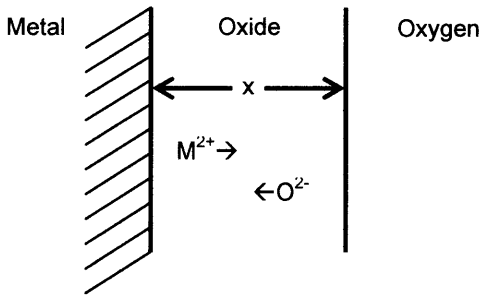

Figure 1.2: Features of a metal undergoing thermal oxidation in oxygen

Metal oxides can be classified as a series of semiconductors to facilitate description and modeling. However, there can be no net current flow through the oxide film. Using the layout in Figure 1.2 with the metal on the left hand side and the oxygen atmosphere on the right; the flow of positive current to the right in the form of a cation flux must be balanced by a flow of negative current anions (leftward flow). Electron transport occurs by movement of free electrons in *n*-type oxides and by electron holes in *p*-type oxides. Electron holes migrate by electron transfer between stationary neighboring metal cations. The concentration of dominant oxide defects, namely cation interstitials, anion vacancies, and cation vacancies affect the diffusivity (thus, the rate) of oxidation. Electrons or electron holes migrate much faster than ionic defects.

Naturally, every kind of defect can be present in all oxides, but usually one predominates in any particular oxide. For this reason, classification of an oxide is facilitated by focusing on their predominant defects, as in Table 1-1. The oxides in bold font are those most closely related to the alloys in this work. Furthermore, Schottky defects are included for completeness, but the discussion is focused on the *n*- and *p*-type semiconductors.

Table 1-1: Classification of various oxides by defect structure[10]

Defect	**Conduction**	**Oxides**
Schottky	ionic	MgO, **Al_2O_3** (T<825 °C)
Cation vacancies	p-type	**FeO**, **NiO**, MnO, CoO, Cu_2O, **$FeCr_2O_4$** , UO_2
Cation excess	n-type	ZnO, CdO, BeO, Al_2O_3 (T>825 °C), $MgAl_2O_4$, UO_3, U_3O_4
Anion vacancies	n-type	TiO_2, ZrO_2, **Fe_2O_3***
Mixed	mixed	**Fe_3O_4**

*with some cation interstitials

***n*-type oxides:**

These oxides can be further classified as a cation interstitial system and an anion vacancy system. The *n*-type oxide treats the oxidation process at the metal/oxide interface as the simultaneous conduction of electrons and injection of metal cations into the oxide.[11] The concentration of conduction electrons within the oxide is not large because of the nature of the energy band gap between conduction levels of the metal and oxide. A large energy band gap will classify the oxide as an insulator and one with an intermediate band gap will be classified as a semiconductor.[12] The highest filled level in the adsorbed oxygen is lower than the conduction level of the metal, which causes conduction electrons from the metal to be drained off by the oxygen, effectively ionizing the oxide. This reduction of oxygen makes the potential at the oxide/oxygen interface more negative which raises the electron energy levels. At equilibrium, the highest filled energy states in the metal and oxygen will be the same, maintaining a potential difference across the oxide, with the inner surface of the oxide being positive with respect to the outer surface. This potential gradient results in the metal cations being driven towards the negative oxide/oxygen interface.

***n*-type cation interstitial oxide system:**

This reaction experiences a concentration gradient in which cation interstitials diffuse from the metal/oxide interface, where they enter, to the oxide/oxygen interface, where they are consumed. Interstitial cations, M_i^{2+}, are the dominant oxide defects.[13] These cations are liberated at the oxide interface by the anodic reaction (1), and then migrating to the oxide/oxygen interface by jumping to adjoining interstitial positions will undergo the reaction in (2) to form oxygen anions at the surface. The oxygen anions react to form surface oxide by reaction (3).

$$M \rightarrow M^{2+} + 2e^- \quad (1)$$

$$\tfrac{1}{2}O_2 + 2e^- \rightarrow O^{2-} \quad (2)$$

$$O^{2-} + M_i^{2+} \rightarrow M_{ox} + O_{ox} \quad (3)$$

M_{ox} and O_{ox} represent metal and oxygen, respectively, incorporated into the oxide lattice. The oxidation reaction in (1) also liberates electrons which can migrate to the oxide/oxygen interface and contribute in reaction (2). Oxidation in this system proceeds if the oxygen pressure exceeds the dissociation pressure of the oxide, i.e., if $p_{atm} > p_o$. This process is illustrated in part (a) of Figure 1.3.

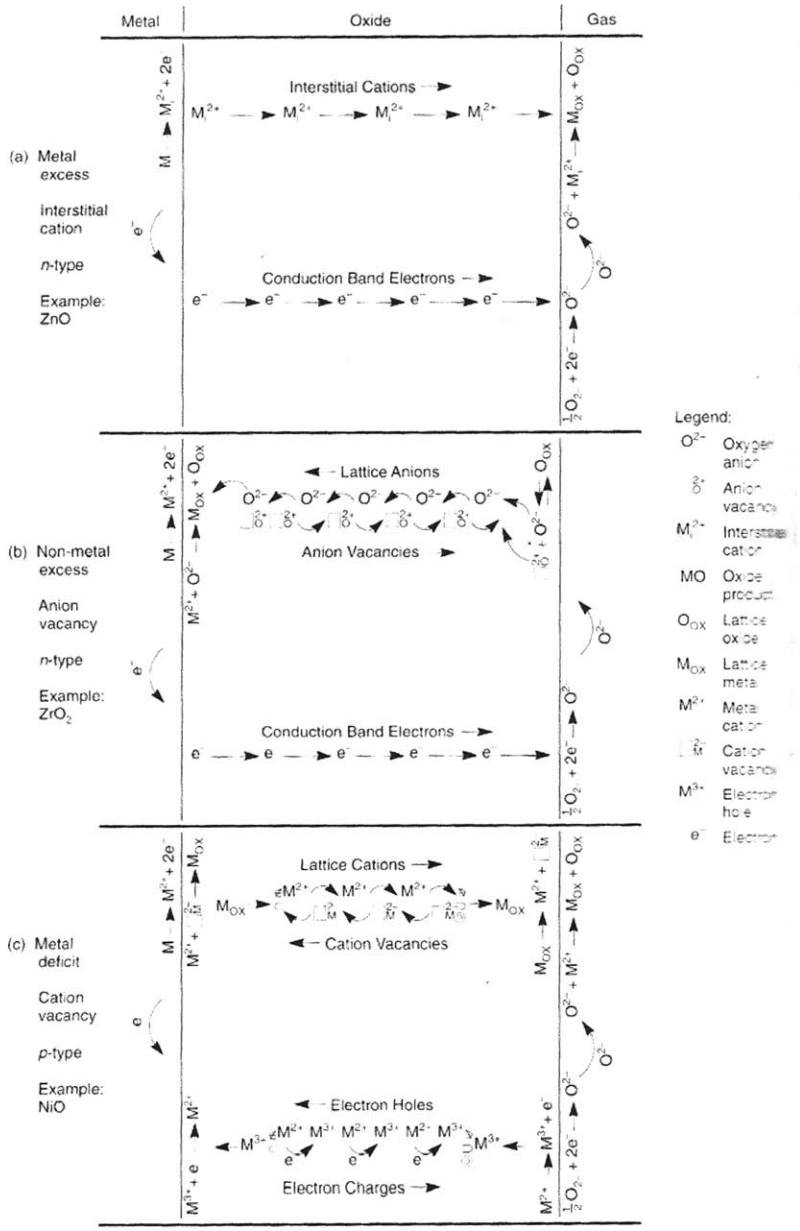

Figure 1.3: Processes occurring during high temperature oxidation[14]

***n*-type anion vacancy oxide system:**

The concentration gradient for this type of reaction causes anion vacancies to diffuse from the metal/oxide interface to the oxide/oxygen interface.[15] Anion vacancies are the dominate oxide defect in this type of oxide. Oxygen anions migrate from the oxide/oxygen to the metal/oxide interface by anion vacancy exchange where they reaction with the metal cations by reaction (4).

$$O^{2-} + M^{2+} \rightarrow M_{ox} + O_{ox} \qquad (4)$$

Reaction (3) and (4) are chemically equivalent and only differ by location: Reaction (4) occurs at the oxide/metal interface, whereas reaction (3) occurs at the oxide/oxygen interface. The main diffusion mechanism difference between reactions (3) and (4) is that diffusion for reaction (3) occurs by interstitial exchange while reaction (4) occurs via vacancy exchange. Anion vacancies, $\square_o^{2+}$, enable oxygen anion migration in this oxygen deficient oxide lattice.

The anodic reaction in (1) provides the M^{2+} cations at the oxide/metal interface for reaction in (4) and the electrons for the reaction in (2). The O^{2-} anion formed by reaction (2) is incorporated as O_{ox} in the oxide lattice by combining with an anion vacancy by reaction (5). This exchange between oxygen anions and anion vacancies enables migration of O^{2-} to the oxide/metal interface.

$$\square_o^{2+} + O^{2-} = O_{ox} \qquad (5)$$

This process is illustrated in part (b) of Figure 1.3.

***p*-type oxides**

The *p*-type treats the oxidation and growth process as a transport of electron holes.[16] The adsorbed oxygen accepts electrons from the valence band of the oxide, which creates holes at the oxide/oxygen interface. These holes migrate towards the metal/oxide

interface while the cations migrate towards the oxide/oxygen interface. The holes accept electrons from the metal enabling injection of cations into the oxide. In this system cation vacancies are the dominant defect. Metal cations, M^{2+}, are provided at the oxide/metal interface by the oxidation reaction in (1). These cations migrate to the oxide/oxygen interface by exchange with cation vacancies, $\square_M^{2-}$. This reaction is depicted in (6). The $M_{ox} + O_{ox}$ oxide is formed with the metal cations from reaction (3).

$$M_{ox} = M^{2+} + \square_M^{2-} \qquad (6)$$

M^{3+} electron holes migrate to the oxide/metal interface to the oxide/oxygen interface by accepting electrons from neighbor M^{2+} cations via reaction (7). Only electron transfer is required for electron hole migration. After the M^{3+} reacts with the metal/oxide interface they are converted to M^{2+} cations by accepting the electrons generated in reaction (1).

$$M^{2+} = M^{3+} + e^- \qquad (7)$$

Oxidation proceeds if $p_{atm} > p_0$, i.e. if the oxygen pressure exceeds the dissociation pressure of the oxide. This process is illustrated in part (c) of Figure 1.3.

High Temperature Oxidation of Fe-Ni-Cr Alloys

Very seldom is oxidation of a pure metal of primary interest. Rather, oxidation of steels and other engineering alloys is most important. Plain carbon steels typically contain small concentrations of carbon, manganese, silicon, and excess aluminum. Alloy steels, especially high grades of stainless steel, may contain increased concentrations of the above listed elements in addition to nickel, chromium, molybdenum, and vanadium as alloying components. These additions of various elements affect the driving forces of oxide formation discussed in the above oxide types. However, it is more common for alloyed elements, namely chromium, to form its own protective oxide on the surface of the alloy.

Minimizing oxidation of metal is of primary concern for engineering alloys. The oxidation rate of an alloy will be minimized if it forms a protective oxide, which has the following properties:

1. Strong adherence to the base metal to prevent flaking and spalling.
2. The film should have low electrical conductivity and low diffusion coefficients for metal ions and oxygen.
3. High melting point.
4. Low vapor pressure to resist evaporation.
5. The oxide film and metal should have close to the same thermal expansion coefficients.
6. The film should have high temperature plasticity to accommodate differences in specific volumes of oxide and parent metal and differences in thermal expansion.

The alloys covered in this work are focused on the chromium and nickel rich alloys; however, some of the smaller alloying components are also important. Chromium, aluminum, nickel, and silicon are the few elements known for their effective formation of protective high temperature oxides. Other criteria, such as pressure and water content may play a role in enhancing or degrading oxides, as these will determine the redox reactions that can occur.

1.4.2 Pressure

The effect of pressure is most closely tied to dictating the partial pressure of trace impurities such as carbon monoxide or water in the CO_2. It is known that increased water content is adverse to the weight gain characteristics of the Fe-9Cr steels, but a quantitative model for pressure vs. weight gain (possibly as a function of moisture content) has not been performed and the results are currently unknown.[17,18] However, for a constant temperature, increased pressure of CO and O_2 results in an increased thermodynamic driving force to form an oxide.

1.4.3 Water content

Increased water content increases the weight gain of Fe-Cr steels in CO_2 atmospheres and is closely tied to the system pressure. It has been shown that the weight gain is proportional the square root of material thickness.[19] However, this is a function of the purity of the CO_2 and can be controlled by stringent purity guidelines.

1.4.4 Protective oxidation

Fortunately for most engineering applications today many metals/elements tend to form highly stable and protective oxides. A protective oxide is one that is thin, stable, and dense. For example, iron forms an oxide but it is of low integrity; therefore, iron requires additional alloying elements to improve the protective oxidation characteristics. The most common alloying elements to improve oxidation are chromium and nickel because they promote the formation of protective oxide layers. Protective oxide formed on Fe-9Cr steels in CO_2 environments takes the form of a duplex oxide.[20] The outer layer of the duplex layer is formed due to reaction with the bulk gas. The initiation and growth of the inner layer occurs as preferred growth at the metal-oxide interface with some growth throughout the inner layer. The inner layer growth occurs in a striated nature as CO_2 diffuses through both oxide layers and reacts at the metal-oxide interface, which also results in excess carbon deposition and carburization of the underlying metal.

Duplex scale is the predominant protective oxide formed on Fe-9Cr steels in CO_2 environments at temperatures ranging between 400°C and 650°C.[21] The outer layer consists of magnetite Fe_3O_4 and the inner layer is a mixed Fe-Cr spinel, with the oxides being of approximately the same thickness. The duplex scale formed at these elevated temperatures is very similar to the oxide formed on mild steel before breakaway (the point at which the oxide cracks due to mismatch between the volume of the oxide and the metal that was consumed to form the oxide). However, at elevated temperature the material also exhibits an internal oxidation layer, which transforms from a duplex oxide to one with a third component within the protective oxide.

The outer layer of magnetite is comprised of columnar crystals formed by the following reaction:

$$3Fe + 4CO_2 \rightarrow Fe_3O_4 + 4CO \qquad \text{(Eq. 1.2)}$$

The inner spinel oxide layer will form via the following reaction:

$$3M + 2CO_2 \rightarrow M_3O_4 + 2C \qquad \text{(Eq. 1.3)}$$

Where M represents an alloying element that contributes to the spinel oxide. The carbon monoxide from the first reaction will become dispersed in the bulk fluid and will contribute to the carbon deposition via the Boudouard reaction:

$$2CO \rightarrow C + CO_2 \qquad \text{(Eq. 1.4)}$$

The carbon deposition leads to carburization in the metal can develop concentrations beneath the oxide layers that far exceed that which could have been present due to preferential diffusion of carbon in the original alloy. In sufficient quantity, the additional carbon can react with chromium to form chromium carbides depleting the surrounding matrix of chromium.[22] This sensitization contributes to the degradation of the protective oxide by preventing the formation of a continuous Cr_2O_3 scale. The protective oxide layer remains stable until the metal-oxide interface becomes saturated with carbon. Additional carbon results in more porous and a less protective oxide structure.

Due to the temperature ranges of interest in this work, it is important to note the regions of stability for each oxide layer. The three main oxides pertinent in this work are magnetite, wustite, and spinel. Magnetite is thermodynamically stable up to approximately 570 °C, at which a phase change to wustite occurs. Wustite is stable from 570°C to approximately 920°C, as seen in the iron-oxygen phase diagram in Figure 1.4. Of course, other phases are stable within these temperature ranges at higher oxygen partial pressures. The spinel phase is more stable and protective than wustite or

magnetite due to its higher chromium content. However, the outer layer of wustite or magnetite is of little protective quality and the spinel acts as the main corrosion barrier. The region of interest for the oxidation in this work is at lower oxygen content.

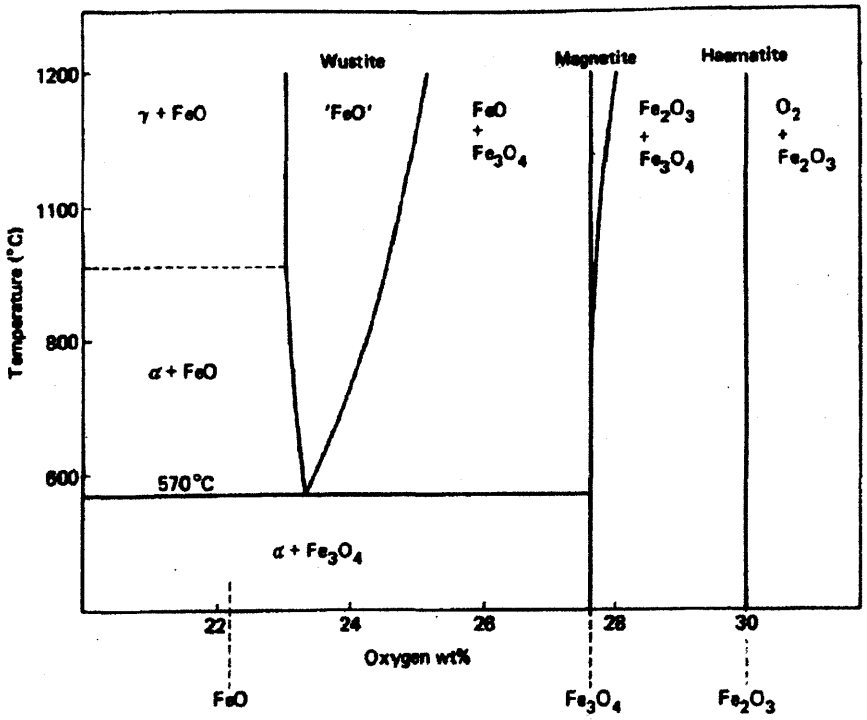

Figure 1.4: Iron-oxygen phase diagram[23]

The morphology and structure of the oxide layer(s) in each alloy plays an important role in the corrosion susceptibility in the S-CO_2 environment. The outer oxide layer is formed by outward diffusion of metal ions (primarily iron, chromium, or nickel in this work) and reaction with oxygen at the surface. The most common oxides present in the iron based alloys in this work are magnetite, wustite, and chromium oxide. The nature of layers as a function of time and composition for oxidation in gas atmospheres has been extensively studied.[24,25,26,27,28] Figure 1.5 shows the parabolic rate constant for the iron-chromium system as a function of chromium concentration for 1000°C. Alloys containing no chromium can form three iron-oxides: Hematite Fe_2O_3), magnetite (Fe_3O_4), and wustite (FeO). Increasing the chromium content will allow for chromium oxide to form. Alloy Fe-2Cr forms a thin layer of iron-chromium oxide at the metal/oxide interface beneath the three iron oxides. Increasing the chromium content further will result in an iron-

chromium spinel forming below magnetite in the Fe-9Cr system. The stainless steel alloys begin when the chromium content exceeds 10-12 wt%. The Fe-16Cr system forms a multilayer oxide consisting of several iron oxides and chromium oxide (Cr_2O_3). The steady-state oxide morphology is multilayer until the chromium concentration exceeds approximately 20-25% where chromium oxide (Cr_2O_3) is the only oxide present.

The type and sequence of oxide layers depend on the partial pressure of oxygen and can be predicted. Naturally, the most oxygen-deficient oxide will reside next to the base metal and the most oxygen-rich oxide will be on the surface reacting with the working fluid. In the iron-oxygen system, the sequence from the innermost to outermost oxide layers is FeO, Fe_3O_4, and then Fe_2O_3.[29] However, this does not imply that each of these oxides will be present; each oxide is only stable over a particular temperature range and, depending on the exposure temperature, only those thermodynamically stable may form. The relative thickness of each of these oxide layers should be proportional to the relative diffusion rates that generate each layer.[30] The thickness ratio of a two oxide layer system tells a lot about the ongoing processes. If the thickness layer (inner to outside layer) is less than unity this implies that the diffusion rates for ions that create the inner layer (oxygen anions in this case) should be less than those that create the outer layer (iron ions).

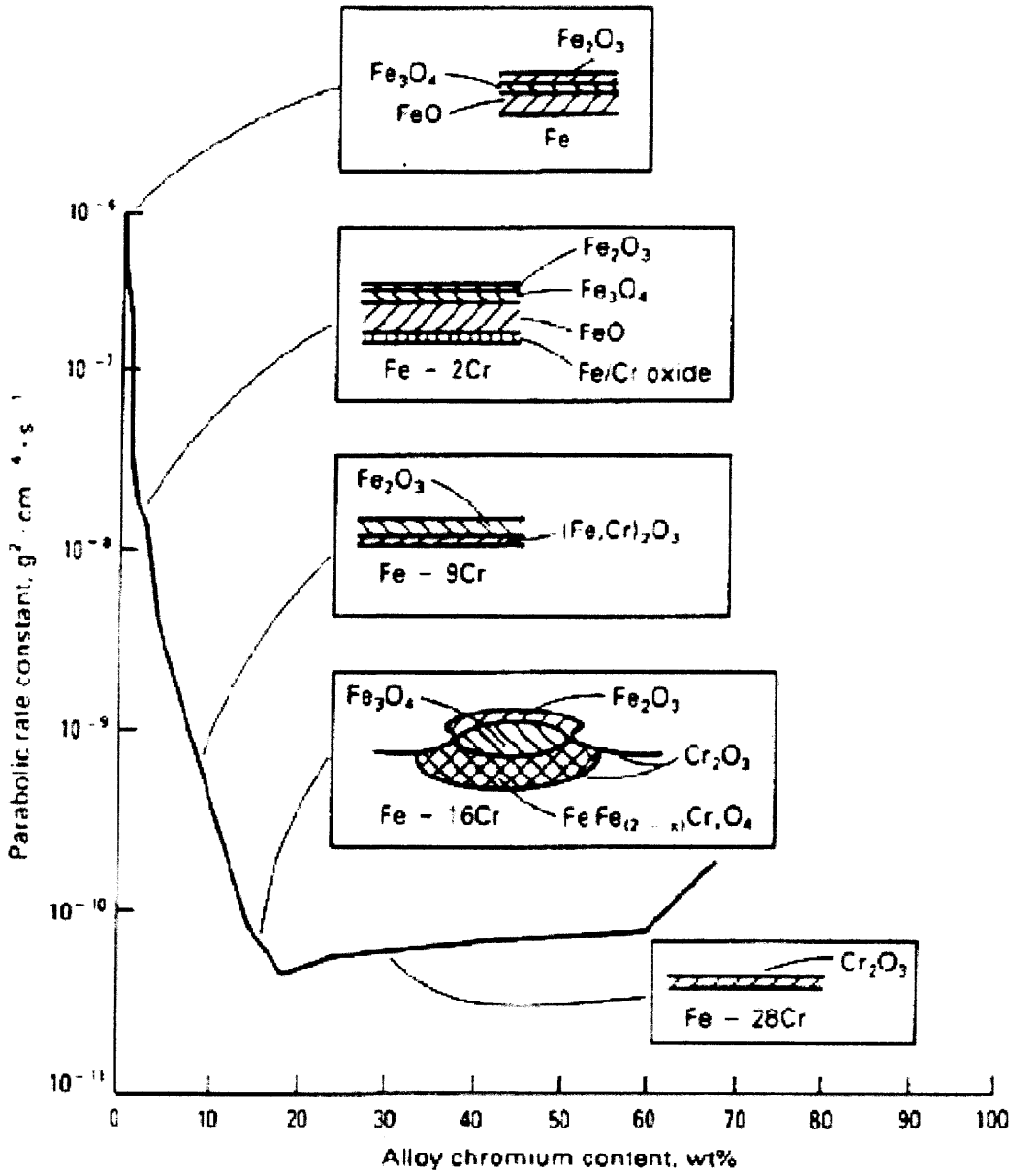

Figure 1.5: Effect of Chromium Concentration on Oxidation Rate and Structure[31]

Magnetite is formed and is stable between 400-570°C. The magnetite layer contains high porosity, which enhances diffusion, and is undesirable. The temperature of interest in this work was 610°C, which is a thermodynamically unstable region for magnetite. Thus, wustite is the most likely oxide layer, as it is stable above about 570°C. It is, however, possible, for a multi layer oxide to form, as the operating temperature is close to the transition temperature between magnetite and wustite and the actual test temperature may

have been actually closer to this transition temperature than initially expected.[1] Thus, the inner oxide layer can initially form as a $(Fe,Cr)_3O_4$ spinel by inward diffusion of oxygen to the oxide-metal surface if the chromium content is sufficiently high (>9wt%). This oxide layer would form first, albeit, may be very thin, as the system temperature is raised to the test range. Above 570°C, when wustite becomes stable, (Fe,Cr)O regions form at the metal-oxide interface.

1.4.5 Pilling-Bedworth Ratio

The Pilling-Bedworth[32] ratio is often used to classify the oxide scales in terms of susceptibility to cracking. Like most covalently and ionically bonded materials, oxides are much stronger in compression than in tension. Oxides under tensile loading are more susceptible to cracking and spallation than those in compression. An oxide will be in tension if it grows at the metal/oxide interface (as opposed to the oxide/oxygen interface) and has a greater specific volume that the metal. Pilling and Bedworth first proposed the ratio of oxide to metal volume as a measure of protectiveness. The ratio is as follows:

$$PB\_ratio = \frac{Wd}{nDw} \qquad \text{(Eq. 1.5)}$$

The quantity (Wd) represents the volume of the oxide produced and the quantity (nDw) represents the volume of the metal consumed. The variable W is the molecular weight and d is the density of the oxide. The variables D, and w are the density, and molecular weight of the pure metal, respectively. The variable n is the number of metal atoms in the oxide molecule, e.g. n=2 for Cr_2O_3. Pilling and Bedworth suggested that an ideal oxide would have a PB ratio slightly higher than 1.0 to foster a moderate compressive stress within the oxide. Several select values of oxides and their PB ratio are recorded in Table 1-2.

[1] After this work was completed, it was determined that the temperature of the samples in the autoclave were slightly higher than 600°C, and not at 650°C, which was the target temperature.

Table 1-2: Pilling-Bedworth Ratio of several oxides

Metal	Oxide	PB Ratio
Aluminum	Al_2O_3	1.28
Chromium	Cr_2O_3	2.02
Iron	FeO	1.78
Molybdenum	MoO_3	3.27
Nickel	NiO	1.70
Titanium	Ti_2O_3	1.76

However, it should be noted here that the PB ratio is rarely applicable to engineering applications as a measure of a protective oxide because it relates the oxide forming on the pure elemental form, e.g. Cr_2O_3 forming on chromium. The PB ratios of higher value are those calculated for an oxide growing on a specific alloy. For example, the PB ratio of chromium oxide (Cr_2O_3) on pure chromium is 2.02, which would be considered too high of a ratio for a protective oxide. On the contrary, chromium oxide is widely known for its desirable protective qualities on stainless steel.

1.4.5 Breakaway oxidation

Breakaway oxidation is a condition where rapid oxidation occurs. Some metals exhibit protective oxidation behavior and then once the oxide reaches sufficient thickness breakaway oxidation sets in. This is marked by rapid weight gain and a rapid thickness increase, usually leading to oxide spallation. The breakaway oxidation characteristics are caused by the striated nature of the inner spinel oxide and the carburization which leads to the $M_{23}C_6$ carbides. When breakaway oxidation occurs post mortem analyses have shown that the carbon levels are never less than 3.5% in the metal beneath the broken oxide scale.[33] The carbon produced during the oxidation is absorbed into the scale. This diminishes adherence and increases porosity. Other general features that affect the time before breakaway include:

1. Temperature: breakaway is reached sooner at higher temperatures
2. Silicon content: increased Si increases the duration within the protective oxide regime by decreasing oxidation rates. This results in an increase in the time to breakaway oxidation.
3. Gas composition: increased water and carbon monoxide content reduces the time to breakaway

4. Specimen geometry: oxides grow faster for regions of higher surface to volume ratio. Breakaway occurs in order for corners, edges, surfaces, respectively.

1.4.6 Kinetics of Fe-9Cr steel oxidation Models:

The Fe-9Cr steel in this work corresponds to Alloy F91. The general model for protective oxide growth for this material varies between a cubic and parabolic kinetics curve of the form:[34],[35]

$$w=at^b \qquad \text{(Eq. 1.6)}$$

where w is the total weight gain and b is generally between 0.3 and 0.5. The constants a and b are dependent on temperature and material composition. Once the protective oxide growth is complete and the oxide transitions into the breakaway region the kinetics are modeled by the linear rate form:

$$w=kt_0 \qquad \text{(Eq. 1.7)}$$

where t_0 is the time to breakaway and k is dependent on temperature, gas composition, and silicon content. Figure 1.6 is an illustration of the weight gain vs. time for protective oxide growth transitioning into breakaway growth.

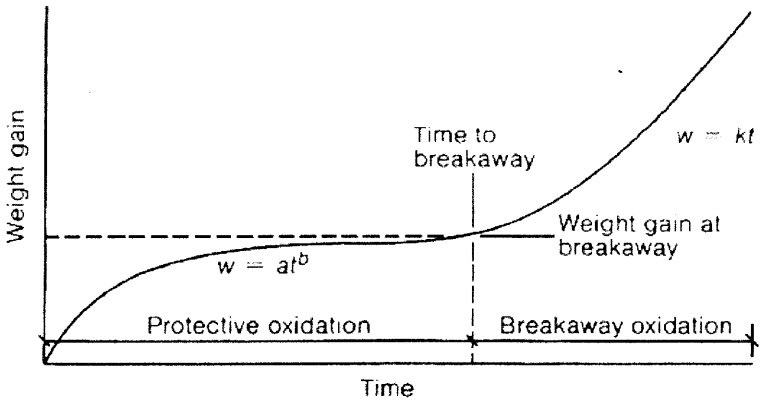

Figure 1.6: Diagram of oxidation leading to breakaway growth[36]

It has been shown that the thickness of the outer magnetite layer has little effect on the oxidation kinetics and that the rate-controlling process is the diffusion of iron ions

through the inner oxide layer.[37] The rate controlling process in duplex oxidation is the outward diffusion of the metal cations. The inner layer is formed in the space vacated by the outward diffusion of the cations; thus, the inner layer is formed in a reduced stress condition. However, premature oxidation failure can occur if the growth of the inner oxide layer is too rapid, resulting in an increased stress state. Furthermore, upon cooling, if the oxide layer is too thick, or grew in a higher stress state and yet unruptured, the oxide is susceptible to cracking when cooled from operating temperature due to the coefficient of expansion mismatch between the two oxide layers and the base metal.

1.5 Oxidation Examples in CO_2

1.5.1 Oxidation of Ferritic Fe-Cr Steels in CO_2

Ferritic Fe-Cr steels consist of chromium and other minor constituents in the body centered cubic structure of ferrite iron. The ferritic Fe-9Cr steels have been the most thoroughly studied, and subsequently the best understood, due to their extensive use in the AGRs. Alloy HCM12A, which is studied more closely in this work, has a structure and composition that falls into this category. Another ferritic steel previously studied in this environment is HT9. However, this alloy underwent undesirable levels of spallation with oxide growth rates more than double that of nickel alloys and austenitic stainless steels (ASS).[38,39,40] However, Alloy PE2000, a rare-earth stabilized, ferritic steel exhibited desirable corrosion behavior in the S-CO_2 environment.

Effect of Chromium

Oxidation behavior of Fe-Cr steels is strongly dependent upon the chromium content. Steels containing less than 9-12% Cr form a duplex scale comprising an outer layer of iron rich oxide and an underlayment of chromium-iron spinel.[41],[42] The duplex spinel oxide grows at a faster rate than the Cr_2O_3 oxide. It is uncommon for ferritic steels with chromium content less than 12% to grow a Cr_2O_3 oxide. Ferritic steels with chromium content between 12-20% form a single Cr_2O_3 layer or a duplex spinel oxide and ferritic steels with greater than 20% will only form a single Cr_2O_3 layer. Ferritic steels utilizing 2-4% aluminum and 10-12% chromium develop Fe-rich oxide scales, but there is also a

competing balance between Cr and Al: If the aluminum content is increased to 6-8% α-Al_2O_3 will form instead of the Fe-oxides.

Effect of Silicon

Silicon has a very significant influence on the growth and stability of the oxide layer. The Fe-9Cr steels alloyed with small amounts of Si (0.06%) have been shown to reduce the oxidation rate and increase the time required to reach breakaway growth behavior.[43,44] It has been shown that ferritic steels with greater than 0.45 wt% Si experienced remarkably lower oxidation rates after 30,000 hours at 500 °C in the AGR reactors. However, Fe-9Cr steels without silicon have experienced breakaway oxidation after 4000 hours at 560 °C. Silicon is present in the spinel oxide (inner) layer and not in the outer magnetite layer. Furthermore, the silicon presence has been shown to shift the distribution of growth rates of the spinel oxide layer towards the metal-oxide interface.[45]

At high temperatures (>550°C) Ferritic Fe-9%Cr steels exhibit non-protective linear oxide growth, which is also known as breakaway oxidation. These conditions would lead to premature component failure due to the unstable oxide growth and resulting weight loss upon oxide spallation.

Effect of Sulfur

Sulfur plays an important role in the oxidation of iron-chromium steels by lowering the oxidation rates with increased content. Similar to silicon, it has been shown that increasing sulfur content up to 0.24wt% reduces the oxidation of 9% chromium steels in CO_2 at 550°C. Sulfur content becomes more important than silicon in controlling the oxidation rate at elevated temperatures. Similar to silicon, sulfur does not affect the outer magnetite or wustite layer and is only present in the Fe-Cr spinel layer.[46] However, sulfur is very detrimental to mechanical properties results reduced ductility for many steels and other alloys.[47] Moreover, sulfur is known to lower the ductile-to-brittle transition temperature. Sulfur is primarily in the form of sulfide inclusions.

1.5.2 Oxidation of Austenitic Alloys in CO_2

Austenitic stainless steels are Fe-Cr steels containing a maximum 0.15wt% C, a minimum of 16wt% Cr, and a face centered cubic (FCC) structure. These steels are known for their high temperature strength and beneficial corrosion properties.[48] In S-CO_2 environments several reactions commonly occur to transfer carbon and oxygen to and from the metal:

$$M + CO_2 \rightarrow MO + CO \qquad \text{(Eq.1.8)}$$

$$2M + CO_2 \rightarrow 2MO + [C] \qquad \text{(Eq. 1.9)}$$

$$M + CO \rightarrow MO + [C] \qquad \text{(Eq. 1.10)}$$

Carbon diffusion into the base metal can result in carbide formation, but once a protective oxide layer has been established these reactions cease. Higher chromium content (in comparison to ferritic steels) enables Cr_2O_3 formation, which is a highly protective oxide due to its stability and density. Sufficient diffusion of carbon into the host metal, before a protective oxide has had time to form, may prevent the Cr_2O_3 protective oxide from forming. This was demonstrated in a laboratory experiment where a thin (100 μm) ASS foil was oxidized in a CO_2 environment at 600°C and resulted in carbide formation and prevention of the protective oxide.[49] However, a longer term issue may stem from using ASS at high temperatures. Sensitization of ASS occurs over the temperature range of 425-815°C. Chromium is depleted from the bulk matrix and forms insoluble carbides ($Cr_{23}C_6$ or Cr_7C_3) on the grain boundaries. Sensitization can be prevented by alloying ASS with niobium or titanium. The ASS tested in this work are susceptible to sensitization. The carbide formation from the reactions governed in equations 1.8-1.10 did not result in breakaway oxidation. Thus, although sensitization may occur at continued operation above 425°C, it is not expected that any carbide formation will contribute to breakaway oxidation because the remaining chromium content is sufficient to maintain a protective oxide layer.

A duplex spinel oxide has also been known to form if chromium depletion on the surface enables an initial layer of iron oxide. However, the duplex spinel oxide is eventually stabilized by in inner layer of the Cr_2O_3 oxide. This stabilization, or healing, is dependent on several factors including chromium content, silicon content, surface finish, degree of cold work, and grain size. A thin layer of silicon oxide can form beneath the duplex spinel oxide, further facilitating stable oxide protection. It has been shown that small grained ASS can grow a fully stabilized and protective oxide layer more than four times faster than larger grained ASS.[50] Similarly, recrystallization of surface grains is facilitated with heavy cold working resulting in more stable oxide formation.

The ASS used as structural materials for the AGR operations were predominantly Fe-18Cr and suffered little corrosion over its entire service life. Lower chromium content ASS was used in the high temperature regions of the AGRs and also exhibited exceptional corrosion resistance.[51] Other corrosion laboratory tests have produced favorable results for type 316SS:10,000 hours of exposure at 600°C and 10 MPa resulted in a cumulative weight gain of 10^{-4} g/cm^2.[52]

1.5.3 Oxidation of Nickel Base Alloys in S-CO_2

Nickel-based alloys offer a number of advantages compared to iron based alloys. Many nickel alloys offer superb high temperature strength, good low temperature ductility, and oxidation resistance over a wide band of temperatures. Unfortunately, little experimental data is available for nickel-based alloys for a wide range of carbon dioxide environments. Recent work was completed at MIT investigating the oxidation effects in S-CO_2 conditions. The MIT work focused on nickel-based alloys Inconel 690, 693, 718, 725, 740, and 740+.[53] These tests were conducted for 1000 hours at temperatures ranging from 650-750°C and pressures from 12.5-20 MPa. These nickel-based alloys exhibited formation of a continuous protective oxide. The oxide formation exhibited parabolic kinetics. It was further noted that the weight gain was a mixture of 50% nickel (NiO), 50% chromium (Cr_2O_3) oxide layer. Both nickel and chromium are known for forming

stable oxide layers, which is why alloys with high concentrations of these elements are known for their oxidation resistance. The notable features to the performance of the nickel-based alloys in S-CO_2 was that while they all performed extremely well with little weight gain, the precipitation hardened alloys tended to show additional localized oxidation of the precipitate phases. However, longer term testing (greater than 1000 hours) is necessary to further qualify these promising alloys for service in S-CO_2.

1.5.4 Oxidation of Special Alloys in S-CO_2

For the purposes of this thesis, a special alloy is classified as one that exhibits a special characteristic and does not fall into the typical steel category, such as ferritic or austenitic steels. The literature of oxidation of ODS steels in S-CO_2 environments is very limited due to the ODS materials being metallurgically young. Amongst the ODS Fe-Cr alloys, the 9Cr-ODS martensitic steels and 12Cr-ODS ferritic steels have been developed by the Japan Nuclear Cycle Development Institute for use in nuclear reactors.[54] The MA957 ferritic alloy, developed by Special Metals, Inc., has been previously tested by Lim, et. al,[55] in high temperature CO_2 environments, but is not a focus of this work.

The improvement in oxidation resistance of ODS alloys can be mainly attributed to two effects: Oxide scale adherence and reduction of growth rate. Chromium oxide is the most common oxide in the high chromium ODS steels and greatly improves the ability of an oxide to adhere to the base metal. The better adherence properties also enable the oxide to be more resistant to spallation and more stable through stress cycles. Controlling the growth rate, or more specifically reducing the growth rate, will lengthen the time to breakaway growth and increase the resistance to oxidation.

1.6 Thesis Organization

A brief motivation and introduction was presented in this chapter.

Chapter 2 outlines the experimental setup, procedure, and more details about the alloys tested.

Chapter 3 describes the various alloys tested in this work and contains the experimental results and associated discussion.

Chapter 4 summarizes the most important experimental results and discusses areas for future work possibilities.

1.7 Chapter Summary

This chapter introduced the scope and outline of this thesis and discussed past publications and experiences with engineering alloys in the CO_2 and S-CO_2 environments. A brief discussion of oxidation was presented which included discussing the use of the Ellingham Diagram in predicting possible reactions with CO_2, types of oxidation, and effects of alloying constituents, and other external parameters such as pressure and water content. The corrosion differences between ferritic and austenitic stainless steels were covered. Little discussion was provided for nickel-base alloys and special alloys, such as ODS steels because this area of research is in its infant stages and little material has been published for these alloys. Lastly, the thesis organization and layout was presented.

1.8 References

1. Nuclear Energy Institute website: http://nei.org/resourcesandstats/nuclear_statistics/worldstatistics/, Accessed May 7, 2010.

2. Nuclear Energy Institute website: http://nei.org/resourcesandstats/nuclear_statistics/usnuclearpowerplants/, Accessed May 7, 2010

3. Gibbs, J., "Power Conversion System Design for Supercritical Carbon Dioxide Cooled Indirect Cycle Nuclear Reactors", MIT Thesis, June 2008.

4. Madina, V. Corrosion of Steels in Carbon Dioxide Environments: Literature Review. Massachusetts Institute of Technology, June 2008.

5. Shropshire, D. "Lessons Learned from GEN 1 Carbon Dioxide Cooled Reactors", s.1 :ICONE 12, April 2004.

6. Lim, J. Y., et. al., Corrosion of Materials in Supercritical CO2 Environments, NACE, Corrosion 2008, March 16-20, 2008

7. Dunlevy, M.W., "An Exploration of the Effect of Temperature on Different Alloys in a Supercritical Carbon Dioxide Environment", Master's Thesis, Massachusetts Institute of Technology, September 2009.

8. World Wide Web: http://web.mit.edu/2.813/OldFiles/www/readings/Ellingham_diagrams.pdf, Accessed May 7, 2010

9. Devereux, O.F., "Topics in Metallurgical Thermodynamics", Krieger Publishing Company, Malabar, Florida, 1989.

10. Talbot, D., Corrosion Science and Technology, CRC Press, Boca Raton, Florida, Table 2.11, (1998).

11. Jones, D.A., *"Principles and Prevention of Corrosion, 2nd Ed."*, Prentice Hall, Upper Saddle River, NJ, 1996.

12. Devereux, O. F., *"Topics in Metallurgical Thermodynamics"* Robert E. Krieger Publishing Co., Malabar, Florida, 1983.

13. Jones, D.A., *"Principles and Prevention of Corrosion, 2nd Ed."*, Prentice Hall, Upper Saddle River, NJ, 1996.

14. Jones, Figure 12.13

15. Talbot, D., Talbot, J., "*Corrosion Science and Technology*", CRC Press, Boca Raton, Florida (1998).

16. Jones, D.A., *"Principles and Prevention of Corrosion, 2nd Ed."*, Prentice Hall, Upper Saddle River, NJ, 1996.

17. Franklin, D.G., Lang, P.M., "Zirconium-alloy corrosion: A review based on an International Atomic Energy Agency (IAEA) Meeting: Zirconium in the nuclear industry", 9th International Symposium, Japan, 1998

18. Moseley, P.T., Tappin, G., and Riviere, J.C., "Oxidation of iron-chromium-silicon alloys (CrO and 9wt%, Si-1wt%) in carbon dioxide at 500°C", High Temperatures-High Pressures, Vol. 14, 559-570 (1982).

19. Rowlands, P.C., Garrett, J.C.P., Popple, L.A., Whittaker, A., Hoaskey, A., "The oxidation performance of Magnox and advanced gas-cooled reactor steels in high pressure CO_2", Nuclear Energy, 25, 267-275 (1986).

20. Allen, G.C., Brown, I.T., Wild, R.K., "The early stages of the oxidation of a 9% chromium steel in carbon dioxide studied using imaging SIMS", Materials Science and Technology, 4, 1117-1118 (1988).

21. Ferreira, L.F.R., et. al., "A Study of the Mechanism of Corrosion in Some Ferritic Steels in High Pessure Carbon Doxide with the Aid of Oxygen-18 as a Tracer III. Fe-9%, Cr-1%, Mo-0.26%", Proceedings Roy. Soc. Lond. A, Vol. 422, 279-188 (1989).

22. Stobbs, W.M., Newcomb, S.B., Metcalfe, E., "A microstructural Study of the Oxidation of Fe-Ni-Cr Alloys II. Non-Protective Oxide Growth", Phil. Trans. Roy. Soc (Lond) A, 319, 219-247 (1986)

23. World Wide Web: www.msm.cam.ac.uk/Teaching/pastpapers/2005-II-1.pdf, Accessed May 7, 2010

24. Lai, G.Y., High Temperature Corrosion of Engineering Alloys, ASM International (1990).

25. Talbot, D., Corrosion Science and Technology, CRC Press, Boca Raton, Florida (1998).

26. Kubaschewski, O., Hopkins, B.E., "Oxidation of Metals and Alloys, 2nd ed., Butterworth, London (1962).

27. Robertson, J., Manning, M.I., "Healing Layer Formation in Fe-Cr-Si Ferritic Steels",Mater. Sci. Technol., 5, 741 (1989).

28. Atkinson, A., "A Theoretical Analysis of the Oxidation of Fe-Se Alloys," Corrosion Sci, 22, 87 (1982).

29. ASM Handbook Corrosion: Fundamentals, Testing, and Protection, vol. 13A, ASM International Materials Park, OH, 2003, p. 97

30. Metals Handbook, Corrosion, 9th Ed.., ASM International Handbook committee, Metals Park, OH, 1987.

31. Ballinger, R.G., Lim, J., An Overview of Corrosion Issues for the Design and Operation of High-Temperature Lead- And Lead-Bismuth-Cooled Reactor Systems", Nuclear Technology, Vl. 147, Sept. 2004.

32. Pilling, N.B., Bedworth, R.E., J. Inst. Met., Vol. 29, p. 529, 1923

33. Gleave, C., et. al., "A Study of the mechanism of corrosion of some ferritic steels in high-pressure carbon dioxide with the aid of oxygen-18 as a tracer. I. Low-silicon mild steel" Proc. R. Soc. Lond. A 379, 429-427 (1982)

34. Rowlands, P.C., Garrett, J.C.P., Popple, L.A., Whittaker, A., Hoaskey, A., "The oxidation performance of Magnox and advanced gas-cooled reactor steels in high pressure CO_2", Nuclear Energy, 25, 267-275 (1986).

35. German, P.A,. "Mild steel oxidation in CO2-cooled reactors", Gas Cooled Reactors Today, Proceedings of the conference, Bristol, 20-24 (1982).

36. Rowlands, P.C., Garrett, J.C.P., Popple, L.A., Whittaker, A., Hoaskey, A., "The oxidation performance of Magnox and advanced gas-cooled reactor steels in high pressure CO_2", Nuclear Energy, 25, 267-275 (1986).

37. Pritchard, A.M., et. al., "Oxygen-18 and deuterium profiling in thick films on Fe-9% Cr alloys by 3 MeV nuclear microprobe", Corrosion Science, Vol. 20, 1 (1980).

38. Lim, J.Y., et al., Corrosion of Materials in Supercritical Carbon Dioxide Environments. S.1. : Massachusetts Institute of Technology.

39. Dunlevy, M., et. al., Corrosion of Materials in a Supercritical Carbon Dioxide Environment. Troy, NY: Supercritical Carbon Dioxide Power Cycle Symposium, 2009.

40. Cao, G., et. al., "Corrosion of Candidate Alloy in Supercritical Carbon Dioxide. Troy, NY: Supercritical Carbon Dioxide Power Cycle Symposium, 2009.

41. Ferreira, L.F.R., et. al., "A Study of the Mechanism of Corrosion in Some Ferritic Steels in High Pessure Carbon Doxide with the Aid of Oxygen-18 as a Tracer III. Fe-9%, Cr-1%, Mo-0.26%", Proceedings Roy. Soc. Lond. A, Vol. 422, 279-188 (1989).

42. Allen, G.C., Brown, I.T., Wild, R.K., "The early stages of the oxidation of a 9% chromium steel in carbon dioxide studied using imaging SIMS", Materials Science and Technology, 4, 1117-1118 (1988).

43. Holmes, D.R., Mortimer, D. and Newell, J. Discovery and Assessment of Accelerated Corrosion in Fe-9Cr Alloys and Steels. S.1. : BNES International Conference on Corrosion of Steels in Carbon Dioxide, 1974.

44. Taylor, J.W. and Trotsenberg, P.V. 9Cr-Mo Steels Breakaway Effects in Carbon Dioxide Coolant Media. S.1 :BNES International Conference on Corrosion of Steels in Carbon Dioxide, 1974

45. Mosley, P.T., Tappin, G., Riviere, J.C., "Oxidation of iron-chromium-silicon alloys (CrO and 9wt%, Si 0-1wt%) in carbon dioxide at 500°C", High Temeratures-High Pressure, Vol. 14, 559-570 (1982).

46. Pritchard, A.M., Truswell, A.E., "Mechanistic experiments on the oxidation of 9%Cr steels in CO2 at 550°C", Corrosion of Steels in CO2, BNES (1974)

47. World Wide Web: http://www.materialsengineer.com/E-Alloying-Steels.htm, Accessed May 7, 2010.

48. Thon, Susanna. Selection of Materials for a Supercritical Carbon Dioxide Cooled Gas Fast Ractor. S.1.: CANES, Aug. 2002.

49. Cao, G., et al., Corrosion of Candidate Alloys in Supercritical Carbon Dioxide. Troy, NY: Supercritical CO2 Power Cycle Symposium, 2009.

50. Tripathi, K.C. and Antill, J.E. Influence of Metallurgical Condition and Surface Finish on the High Temperature Oxidation Behavior of Austenitic Stainless Steel in Carbon Dioxide. S.1.: John Wiley & Sons, 1985.

51. Madina, V. Corrosion of Steels in Carbon Dioxide Environments: Literature Review. June 2008.

52. Kato, Y., Overview of Supercritical Carbon Dioxide Cycle Studies at Tokyo Tech. Cambridge, MA: MIT-Tokyo Tech Symposium on Innovative Nuclear Energy Systems, Nov 2-4, 2005.

53. Dunlevy, M.W., "An Exploration of the Effect of Temperature on Different Alloys in a Supercritical Carbon Dioxide Environment", Master's Thesis, Massachusetts Institute of Technology, September 2009.

54. Kaito, T., et. al., "High Temperature Oxidation Behavior of ODS Ferritics", Journal of Nuclear Materials 307-311, 763-768 (2002).

55. Lim, J. Y. et. al., Corrosion of Materials in Supercritical CO2 Environments, NACE, Corrosion 2008, March 16-20, 2008

This page intentionally left blank

Chapter 2 – Alloys and Experimental Procedure

This chapter also contains an introduction and description of each alloy tested in this thesis. This chapter also covers the experimental procedures, which include a thorough description of the initial sample preparation, experimental test apparatus, and post test preparation and analyses.

2.1 Alloys

This section provides further details on the alloys under investigation in this work. This section is divided into five subparts: Austenitic stainless steels; ferritic-martensitic stainless steels; nickel-based, solution-hardened alloys; nickel-based, precipitation hardened alloys; and special steels, namely oxide dispersion steels.

The materials under consideration for use in the S-CO_2 environments can be broadly classified into the following four categories:

1. Ferritic steels: these include martenitic steels up to 12% chromium and an upper useful temperature of 650°C
2. Austenitic stainless steels: These steels are able to maintain high temperature strength typically up to 700-800°C.
3. Nickel alloys: These include solid solution and precipitation hardened alloys that can maintain strength in excess of 1000°C.
4. Special materials: These include oxide dispersion strengthened (ODS) steels and are being designed for strength retention at very high temperatures (>1000°C)

2.1.1 Ferritic Stainless Steels

The ferritic stainless steels (FSS) are body-centered-cubic (BCC) Fe-Cr-C alloys with minor additional constituents alloyed with iron. Chromium serves to enhance corrosion resistance and stabilize the BCC structure. FSS are known for their susceptibility to intergranular corrosion, in addition to the low ductile-to-brittle transition temperatures. These steels are primarily used in sheet and tubular products such as tube-support plates

of pressurized water nuclear reactor steam generators and thin-wall tubing for heat exchangers. The advantage of using FSS is its immunity to chloride-induced stress corrosion cracking (SCC). Ferritic steels include martensitic stainless steels and are used in nuclear engineering applications because their reduced activation and excellent resistance to void swelling make them great candidates for structural components. However, ferritic steels suffer more thermal creep than austenitic steels. Developmental ferritic alloys in the 10-13Cr range exhibit the required strength for temperatures up to about 620°C, for the pressure range of interest in this work, but the low chromium content raise concerns about the high temperature oxidation resistance.

Ferritic/martensitic steels have been widely studied and developed for applications in the energy industry. Their performance in various energy systems has been reviewed by Klueh and Harries.[1] The ferritic/martensitic steels examined in this work are Alloys HCM12A and F91.

Alloy HCM12A

This alloy is a precipitation hardened, martensitic, alloy and is one of the third generation 12Cr ferritic steels[2], which was developed for heavy section components such as headers and steam pipes at temperatures up to 620°C and pressures up to 34 MPa[3]. The design of alloy HCM12A took the following several aspects into consideration. To improve weldability, the carbon content of alloy HCM12A is reduced to about half of the carbon content in the conventional 12Cr ferritic steels, such as T91 that has been extensively used as high-temperature components in power plants.[4] Tungsten, molybdenum, vanadium, and niobium are added to improve creep strength through two strengthening mechanisms: solution strengthening by W and Mo, and precipitation strengthening by V and Nb. The strengthening due to the W has a greater effect on creep resistance than that of Mo. V and Nb precipitate into an extremely fine coherent MX carbonitride on the ferrite matrix. As compared to other widely employed steels, HCM12A employs a lower Ni content to increase the long term strength and further facilitates high-temperature tempering.[5] The general composition of Alloy HCM12A is recorded in Table 2-1.

Table 2-1: HCM12A Composition[6]

Alloy	Element (wt%)
Fe	Balance
Ni	0.34
Cr	12.5
C	0.071
Mn	0.54
Si	0.25
Mo	0.36
V	0.21
Cu	0.85
Nb	0.045
W	1.9

Alloy F91

Alloy F91 is considered a high-chromium, martensitic stainless steel known as heat resistant steel with good creep and rupture properties. The creep resistance is derived by niobium and vanadium precipitation-hardened phase of fine MX carbonitride. The most common uses of this alloy are heat exchanger tubes, pipes for high temperature service, flanges, and plates for pressure vessels. The complete composition is provided in Table 2-2.

Table 2-2: F91 Composition[7]

Alloy	Element (wt%)
Fe	Balance
Ni	0.4
Cr	8.0-9.5
C	0.08-0.12
Mn	0.30-0.60
S	0.1
Si	0.20-0.50
Mo	0.85-1.05
V	0.18-0.25
Nb	0.06-0.10
N	0.003-0.07
Al	0.04 max

2.1.2 Austenitic Stainless Steels

Austenitic stainless steels (ASS) are used extensively for components in nuclear reactors due their corrosion resistance. In addition, the face centered cubic structure of austenitic stainless steels is desirable because they will not undergo a ductile to brittle transition common among body centered cubic alloys in a harsh radiation environment, such as that present inside nuclear reactors. The ASS steels under consideration in this work are 316SS, 310SS, AL-6XN, and 800H.[1]

The austenite stainless steels are a face-centered cubic stainless steel and are widely used in industry. Nickel is added to the iron-chromium steels to stabilize the austenite phase and improves corrosion resistance synergistically with chromium. Other notable additions to ASS are molybdenum, which improves resistance to chloride pitting and SCC. The ASS has been used extensively in electric power plants for turbine blades and vanes, flue-gas desulphurization equipment, condenser tubing, and heat exchangers. Furthermore, ASS have been used in marine atmospheres, to contain industrial chemicals, food processing and pharmaceutical equipment.[8]

The film stability in ASS is sensitive to the temperature and concentration of acids and can serve as an excellent material choice, or a very poor choice. ASS are susceptible to pitting in chlorides and acids can dissolve the protective oxide layer, making many stainless steels incapable of containing many acids, namely hydrochloric acid. However, ASS are resistant to phosphoric acids over a wide range of concentrations and temperatures, but are susceptible to exposure of hydrochloric acid because the chlorides attack the passive layer causing pitting.[9]

Alloys 316SS

Alloy 316 SS is a molybdenum-bearing austenitic stainless steel and is more resistant to general corrosion and pitting/crevice corrosion than the conventional chromium-nickel austenitic stainless steels. Alloy 316SS also offers better resistance to creep, stress-to-rupture, and tensile strength. In addition to the excellent corrosion resistance and

[1] Alloy AL-6XN is considered a super-austenitic alloy and Alloy 800H is an Incoloy, but are grouped with the ASS for discussion.

strength, Alloy 316 also provides excellent fabricability properties. Alloy 316SS was initially developed for use in paper mills, but is now one of the most common stainless steels and is used for applications such as food processing equipment, chemical and petrochemical equipment, boat fittings, heat exchangers, nuts and bolts, springs, and medical implants, just to name a few.[10] The nominal compositions of Alloy 316SS is provided in Table 2-3.

Table 2-3: Alloy 316 Composition[11]

Element	Alloy 316 SS (wt %)
Fe	Balance
Ni	10.0-14.0
Cr	16.0-18.0
C	0.08
Mn	2.0
S	0.03
Si	0.75
P	0.45
Mo	2.0-3.0
N	0.10

*Source: ASTM A240

Alloy 310 SS

This alloy is a stainless steel with slightly higher Cr and Ni content than the 316 series stainless steels. This alloy has excellent resistance to oxidation under constant temperature; however, cyclic conditions reduce the oxidation resistance. Alloy 310 SS has a lower coefficient of expansion compared to most 300 series stainless steels and better creep resistance than the 18/8 stainless steel grades. Alloy 310 is most widely used in moderately carburizing atmospheres such as those in petroleum plants. Furthermore, the high chromium and nickel content allows Alloy 310 SS to be used in atmospheres that contain modest amounts of sulfur. The most common use of Alloy 310 SS for engineering applications is in heat exchanger and heat recuperator tubing. The nominal composition of Alloy 310 SS is provided in Table 2-4.[12]

Table 2-4: 310 SS Composition[13]

Alloy	Element (wt%)
Fe	Balance
Ni	19.0-22.0
Cr	24.0-26.0
C	0.08 (max)
Mn	2.0 (max)
S	0.03 (max)
Si	0.75 (max)
Mo	0.75 (max)
P	0.045 (max)

AL-6XN

This alloy is considered a super-austenitic stainless steel. This alloy exhibits greater resistance to chloride pitting, crevice corrosion, and stress corrosion cracking than the 300 series stainless steels, and is more economical than the traditional corrosion resistance nickel-based alloys. [14] The nominal composition of Alloy AL-6XN is provided in Table 2-5.

Table 2-5: AL6XN Composition[15]

Alloy	Element (wt%)
Fe	Balance
Ni	24.0
Cr	20.5
C	0.02
Mn	0.40
S	0.002
Si	0.40
Mo	6.3
P	0.025
Cu	0.1
N	0.22

Alloy 800H

This alloy is an iron-nickel-chromium alloy with enhanced creep rupture strength compared to Alloy 800. The higher strength is derived from the close control of carbon, aluminum, and titanium content combined with a high annealing temperature. It is not uncommon to have alloy 800H with combined titanium and aluminum levels between 0.85 and 1.2% for enhanced high temperature properties. Alloy 800H exhibits excellent resistance to carburization, oxidation, and nitiriding atmospheres. Moreover, this alloy is able to resist embrittlement after long periods of exposure in 650-875 °C range, which is a common problem with many stainless steels.[16] Typical components constructed of Alloy 800H typically include valves, fittings, and other components exposed to corrosive media up to 600 °C.[17] Moreover, applications for this alloy include hydrocarbon cracking, cracking furnaces for vinyl chloride, ethylene pyrolsis, diphenol and acetic acid. The nominal composition of Alloy 800H is provided in Table 2-6.

Table 2-6: 800H Composition[18]

Alloy	Element (wt%)
Fe	39.5
Ni	32.5
Cr	21.0
C	0.10
Mn	1.5
S	0.015
Si	1.0
Ti	0.60 max
Cu	0.75
Al	0.60 max

2.1.3 Nickel Based Alloys

These alloys include both solid solution hardened and precipitation hardened nickel-based alloys. Solid-solution hardened alloys are typically used where ductility is desired and high temperature strength for long durations is not required. The solid-solution hardened, nickel-base alloys under investigation in this work are Haynes Alloy 230 and Alloy 625. Precipitation hardened, nickel-based alloys are considered superalloys. Typical precipitation hardened alloys are used when high temperature strength and oxidation resistance is required, as in applications such as gas turbine engines.

Precipitation hardened alloys trade ductility for strength, which is derived by using precipitates to restrict dislocation movement. The precipitation hardened, nickel-base alloy explored in this work is PE16.

Haynes 230 Alloy

This alloy is a nickel-based, solid-solution hardened, heat-resistant alloy for applications demanding high strength at high temperatures (creep resistance) as well as corrosion resistance. This alloy is superior to many common Fe-Ni-Cr and Ni-Cr alloys, and displays a superior combination of strength, stability, fabricability, and environmental resistance. Haynes 230 Alloy can be utilized for continuous operation of temperature reaching 1150°C. Furthermore, Haynes 230 Alloy is well designed for and used in combustion environments and nitriding and is recommended for use in nitric acid catalyst grids, high-temperature bellows, and thermocouple sheathing, just to name a few.[19] The nominal composition is provided in Table 2-7.

Table 2-7: Haynes 230 Composition[20]

Alloy	Element (wt%)
Fe	3.0 (max)
Ni	Balance
Cr	22.0
C	0.10
Mn	0.50
Si	0.40
Mo	2.0
Co	5.0 (max)
Al	0.30
B	0.015 (max)
W	14.0
La	0.02

Alloy 625

Alloy 625 is a Ni-Cr alloy used for its high-strength, fatigue and thermal-fatigue strength, excellent corrosion resistance, and ease of fabricability and weldability. This alloy can be use from temperatures ranging from cryogenic to about 975°C. Alloy 625 derives its strength from the addition of molybdenum and columbium to its Ni-Cr matrix. Alloy 625

has good oxidation resistance, pitting, intergranular attack, chloride-induced stress corrosion cracking, intergranular attack, and high-temperature effects such as oxidation and carburization. The good ductility and welding behavior of Alloy 625 make it ideal for all applications for use include structures in contact with seawater, chimney linings, offshore marine equipment, and flue gas scrubber components.[21] The nominal composition is provided in Table 2-8.

Table 2-8: 625 Composition[22]

Alloy	Element (wt%)
Fe	5.0 (max)
Ni	Balance
Cr	20.0-23.0
C	0.10 (max)
Ti	0.40 (max)
Co+Ta	3.15-4.15
Al	0.40 (max)

Alloy PE-16

This alloy was designed as a precipitation-hardened material with excellent hot and cold-working and welding characteristics. Alloy PE16 is a less expensive, lower nickel content Ni-Cr-Mo alloy in the high temperature, high strength alloy category. This alloy derives its high temperature strength from the fine dispersion of aluminum and titanium containing precipitates (γ') and solid-solution strengthening with molybdenum. Alloy PE16 is able to maintain its strength and oxidation resistance up to about 750°C. Common uses are general purpose high temperature applications such as industrial furnace components, structural components in nuclear reactors, and gas turbine hot sections where strength and oxidation resistance are important.[23] The nominal composition is provided in Table 2-9.

Table 2-9: PE16 Composition[24]

Alloy	Element (wt%)
Fe	Balance
Ni	42.0-45.0
Cr	15.5-17.5
C	0.04-0.08
Mn	0.20 (max)
S	0.015 (max)
Ti	1.1-1.3
Mo	2.8-3.8
Zr	0.02-0.04
Cu	0.50 (max)
Co	2.0 (max)
Al	1.1-1.3
B	0.005 (max)

2.1.4 Special Metals

Oxide dispersion-strengthened (ODS) steels were produced with the intent to have higher strength than ferritic steels at high temperatures while maintaining acceptable toughness. The main strengthening mechanism in the ODS steels is derived from a fine distribution of yittria oxide particles. ODS steels are still in an early development stage and continue to exhibit challenges associated with processing and fabrication, especially welding. This category of steels have not yet reached large scale engineering applications and are not being considered for immediate deployment in this project. Nonetheless, testing of ODS steel in high temperature S-CO_2 provides valuable insight to the corrosion properties of bulk ODS materials. The ODS alloy under investigation in this work is Alloy PM2000; however, several other ODS steels are being considered for CO2 cooled nuclear reactors and spallation sources.[25]

Alloy PM2000

Coarse grained PM2000 is an iron-based ODS steel formed by mechanical alloying. ODS steels have been developed for their improved strength and creep resistance at high temperatures. The ODS steels exhibit the high strength of the ferritic steels without the reduced toughness exhibited by many high strength materials. Its high temperature

strength is derived from an even distribution of Y-Ti-O particles throughout the host matrix. This ODS alloy is a class of advanced materials offering both creep- and oxidation-resistance and is used for tubing in a combined-cycle gas turbine (CCGT) heat exchanger in biomass power plants. The complete composition is recorded Table 2-10.

Table 2-10: PM2000 Composition[26]

Alloy	Element (wt%)
Fe	Balance
Cr	20.0
Ti	0.50
Y_2O_3	0.50
Al	5.5

2.2 Sample Preparation

Test samples of each of the ten alloys were provided by Lockheed Martin. Each sample was prepared in the form of circular coupons of approximately 20 mm in diameter by 0.6 mm thick. These samples were prepared in a manner which provided a large surface to volume/edge ratio, namely, a geometry that provided minimized preferential corrosion sites, such as edges. The large surface to volume ratio provides higher accuracy weight gain measurements. All samples were received and tested with a 400 grit finish, which is comparable surface roughness to components deployed for industrial uses. Figure 2.1 provides a photograph of a representative test coupon. The hole at the top of the test coupon is used to suspend itself in the sample train.

Figure 2.1 - Representative Test Coupon

2.3 Equipment

2.3.1 Autoclave

Testing was conducting using a custom built autoclave constructed of Alloy 625. The ends of the autoclave were both penetrated for access and data acquisition into its 2.54 centimeters inner diameter test volume. The overall length is 152 centimeters with a 7.6 centimeter outer diameter. Each end was sealed with a carbon steel bolt connected to an Alloy 625 sealing plug. Two external, fin-type, aluminum heat sinks were employed to dissipate heat from the autoclave outside the furnace and prevent each sealing plug arrangement from overheating. Each heat sink employed 9 fins with the following dimensions: 7.6 centimeters inner diameter, 15 centimeters outer diameter, and 12.7 centimeters long. The outer two aluminum fins were 15 mm thick and the inner seven fins were 6 mm thick. Each fin was 25mm high and was connected to a 7 mm thick, cylindrical base. A picture of the autoclave positioned in the furnace is provided in Figure 2.2.

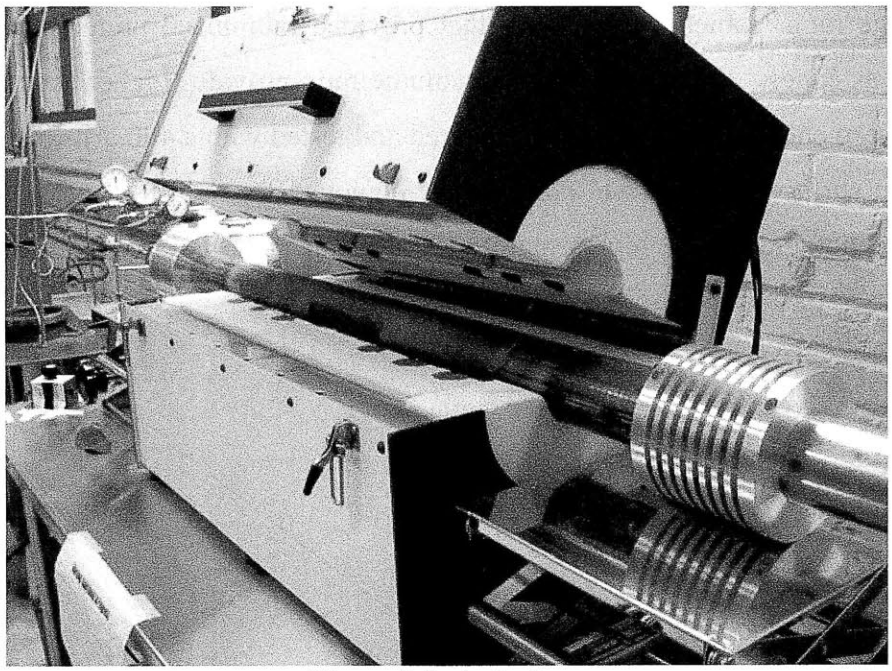

Figure 2.2: Autoclave

2.3.2 Furnace

The autoclave was placed in a 5kW Thermcraft Split Tube Furnace; model number TSP-3.75-0-24-3C-J8927/1A. The furnace employed a Watlow 988B-11CD-AARG

temperature controller to control its three, independent heated zones, and can accurately control temperature to within 1°C. The two outside zones employed a 15 cm heated length and the middle zone had a 30 cm length. The power of each zone linearly varies with the length; the outside two zones each utilized 1250 watts, while the center zone used 2500 watts. The temperature controller used readings from a thermocouple located at the center of each heated zone. Side and end view engineering drawings of the furnace is provided in Figure 2.3. The autoclave height within the furnace was controlled with a small, exterior scissor jack at each end of the furnace.

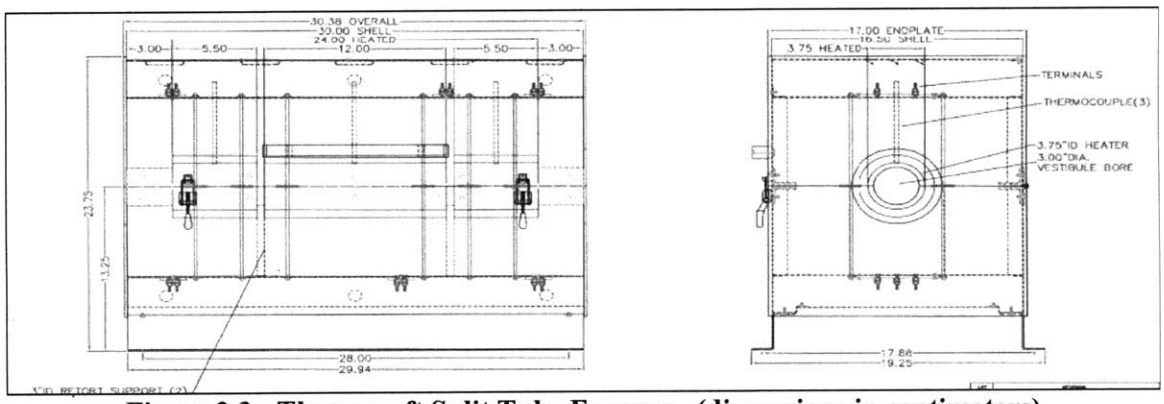

Figure 2.3 - Thermcraft Split Tube Furnace. (dimensions in centimeters)

2.3.3 Sample Train

Sample train components were constructed of 99.7% alumina and were used to suspend and separate the test coupons. An alumina rod was used to suspend the test coupons in the sample train. Each coupon was separated with an alumina washer. A picture of the sample train is provided in Figure 2.4 and its dimensions are recorded in Table 2-11.

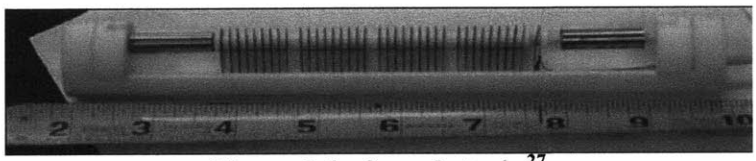

Figure 2.4 - Sample train[27]

Table 2-11: Sample train dimensions

Component	Dimension (cm)
Tube length	20.3
Tube outer diameter	2.4
Rod length	17.4
Rod diameter	0.33
Washer outer diameter	0.56

2.3.4 Data Acquisition

An in-house Visual Basic acquisition program was used on a Dell Precision 420 computer to collect and record the various temperature and pressure readings. The temperature readings were acquired through six K-type thermocouples, which were spot welded to the outer surface of the autoclave. The thermocouple voltages were sent to, and processed with, a National Instruments CA-1000 data acquisition system. The pressure was measured with Omega PX605 and PX615 transducers. The pressure and temperature were also processed with the CA-1000 acquisition system. The CA-1000 data acquisition system interfaced with the Visual Basic program for data monitoring and record.

2.3.5 Experimental Setup

The experimental test system is presented as a line diagram in Figure 2.5. An image of the physical setup in the laboratory is provided in Figure 2.6. The test loop operates in a "feed and bleed" type system with a small feed rate of approximately 320 mL/hr. The CO_2 for the test was obtained from Airgas and was 99.9999% pure with the following certified contaminants: H_2O < 10 ppm, THC < 10 ppm, N_2<70 ppm, and O_2 < 20 ppm, where the units are volumetric parts-per-million. The certificate of analysis for the CO_2 used in this work is provided in the Appendix. The CO_2 was drawn from one of two gas cylinders. The second cylinder outlet pressure was maintained at 4 MPa and was present in the system for redundancy.

The CO_2 was directed from the gas cylinder through ¼ inch type 316 stainless steel tube to either the booster pump or the residual gas analyzer (RGA). The RGA system is a

DYCOR LC100m unit with a Pfeiffer vacuum system. The RGA system was present to monitor and ensure the quality and record of the CO_2 used in the autoclave. The booster pump is a Haskel AGT-15/30, compressed air driven, piston type pump. The booster pump raised the CO_2 pressure from the bottle outlet pressure to the system test pressure, in this case 20 MPa. The booster pump and the downstream tubing were wrapped in Omegalux resistive heating strips to avoid CO_2 condensation at the higher pressure. The CO_2 was directed from the booster pump to the autoclave, in which it flowed around the test specimens. The CO_2 exited the autoclave on the opposite end and was split into two streams; one went to the residual gas analyzer (RGA) to analyze the outlet CO_2 from the autoclave, and the other steam was sent through a liquid seal and was vented into the laboratory. The flow rate of the system was approximated by the bubble stream exiting the liquid seal. A flow rate of approximately one bubble every two seconds was maintained.

The first stream through the RGA was to provide a baseline reading of the CO_2. If any containment were picked up by the CO_2 while traveling through the autoclave they would be identified in the second RGA stream. Each stream to the RGA was reduced to capillary flow, prior to the analysis. The capillary tube reduced the pressure from system pressure to a vacuum, which is necessary for operation. The flow through the capillary tube is dependent upon molecule size, which results in a qualitative sampling of elements. The benefit of the RGA is that it allows comparison between the inlet and outlet CO_2 and indicates if any contaminants are picked up off of the test specimens or autoclave walls. Also, the RGA would record if any reaction produces were formed due to the various chemical reactions.

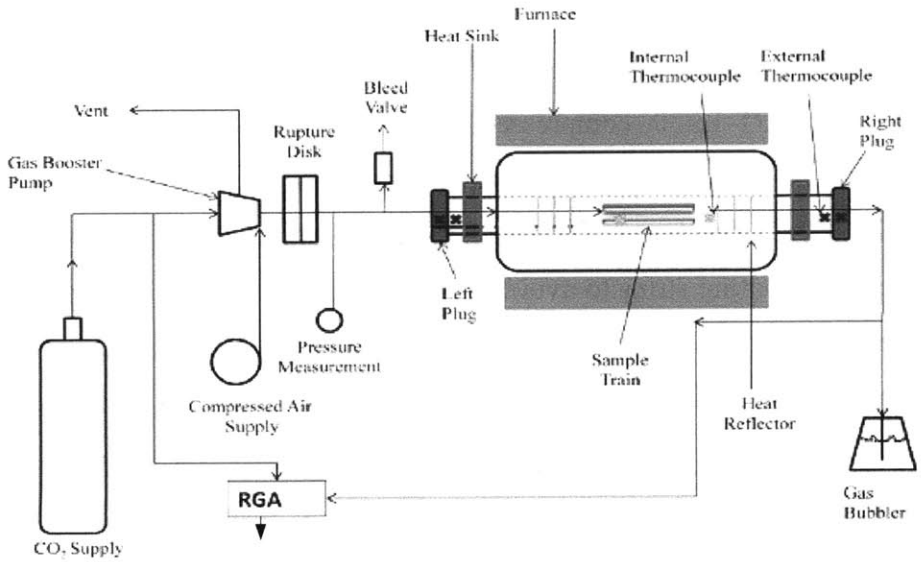

Figure 2.5 - Test system flow diagram

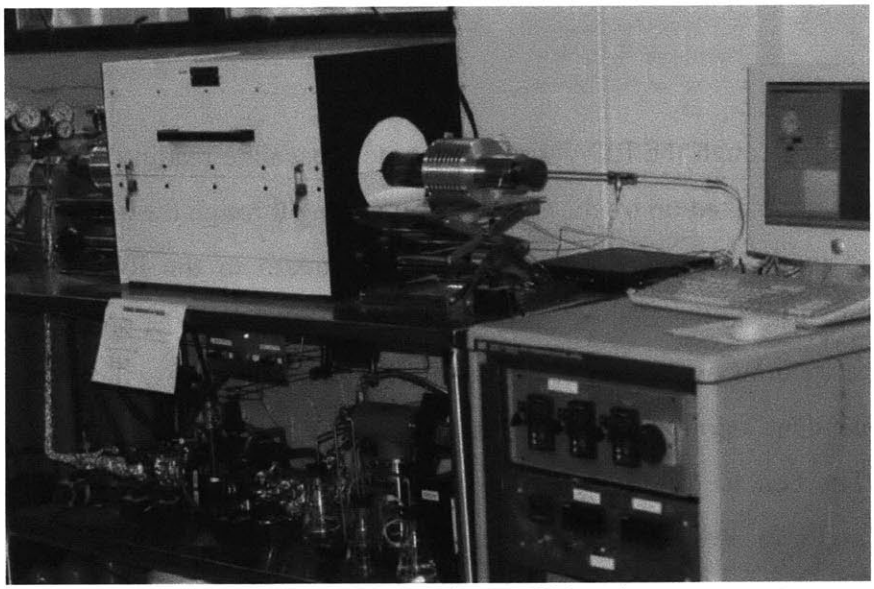

Figure 2.6 - Autoclave Experimental Test Arrangement

2.3.6 Operating Procedure

The operating procedure is broken into several areas: initial specimen placement and system startup, system shakedown, and monitoring.

The initial specimens are placed in the sample train by hanging them from the alumina rod. An alumina washer is placed between each specimen. Next, the specimen tray is slid into the autoclave, along with a thermocouple that measured the temperature at the

midpoint of the end heating zone. The autoclave is sealed by tightening the plug on the inlet. The outlet plug was always kept sealed. The autoclave was then placed into the furnace and the furnace closed. The two scissor lifts were adjusted to ensure the autoclave was not placing its full weight on the vestibules of the furnace. The inlet line, which is connected to the autoclave plug, was reattached to the CO_2 supply system.

Next, the high temperature and pressure alarms were set at 15°C and 1 MPa above their setpoints, respectively. In the event an alarm was tripped due to a temperature or pressure excursion, the system would automatically shutdown. The primary CO_2 cylinder outlet pressure was adjusted to 4.8 MPa via the regulating valve and the secondary cylinder was set to 4.3 MPa. In the event the primary cylinder was exhausted, the secondary cylinder would provide the makeup gas to continue the test. If the primary CO_2 bottle was emptied the overall system pressure would decrease indicating to the monitor that the primary gas bottle needs replenishing. The system high pressure side was set by controlling the air-powered booster pump. At room temperature, the regulator controlling the compressed air was adjusted until the output of the booster pump was 6 MPa.

The system was purged for approximately 24 hours via the feed and bleed method. First the monitoring and recording equipment was started. The system temperature control was set to 140°C. Next, the CO_2 was fed into the system at approximately a flow rate of 1 L/hr. Primarily, the system was purging water vapor from the atmosphere from the autoclave. This was complete once the inlet and outlet RGA data were comparable. The system bleed and feed flow rate was then reduced to approximately 320 mL/hr.

The system was brought up to temperature by increasing the setpoint 200°C every thirty minutes. The slow startup procedure was to reduce the thermal shock on the system and allow system stabilization. Once the system was in stable operation at the designated temperature the pressure was slowly increased. The initial system pressure naturally increased with the stepwise temperature increases. The pressure was not set before the temperature to prevent over pressurization of the system due to the volumetric expansion

of the working fluid when the temperature was increased. The system pressure was raised to the setpoint by controlling the booster pump regulator.

A controlled shutdown of the system progressed by first lowering the system pressure to about 7.5-8 MPa and then stepwise lowering the system temperature. It was important to maintain the temperature and pressure in a manner to remain within the gas stage and prevent CO_2 condensation. Depressurizing the system before lowering the temperature ensured the cool down remained within the gas phase, as seen in the CO_2 phase diagram in Figure 2.7. Any liquid entrainment into the system would disturb the post mortem weight gain measurements. System shutdown typically took more than 24 hours.

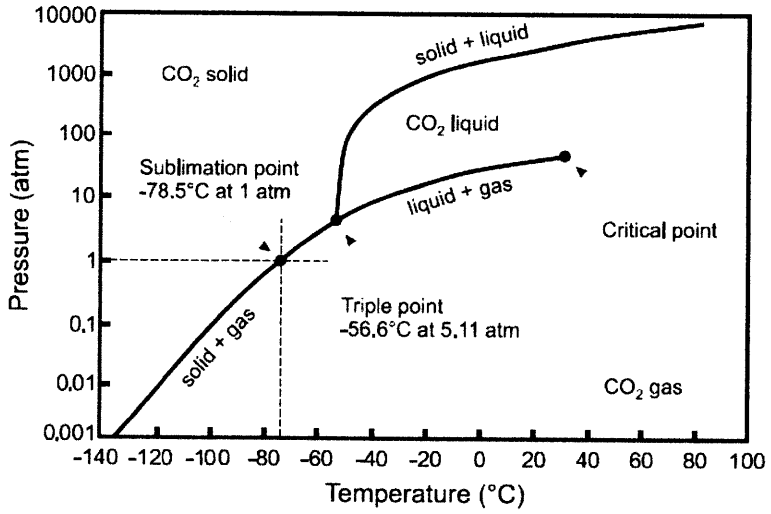

Figure 2.7 - Temperature-Pressure Phase Diagram for CO_2[28]

Upon complete cool down, the samples were then removed from the autoclave and each sample was weighed. For this experiment the tests were run a total of 500 hours per test interval, for a total time of 3000 hours. Each specimen was evaluated at each 500 hour shutdown. Six duplicate coupons of each alloy were mounted on an alumina sample train and tested in the autoclave with one of each coupons removed every 500 hours. Thus, the longest exposure time was 3000 hours. Upon removal from the autoclave, each sample was weighed, and the samples not returned to the autoclave were photo documented.

Furthermore, when the samples were not being processed or analyzed they were stored in a desiccator to prevent atmospheric contamination.

The test were performed at 610°C and 20 MPa, which are the peak nominal operating conditions for the supercritical CO_2 power cycle under consideration in the GNEP program. It should be noted here that after the CO_2 testing for this thesis work was completed it was discovered that the autoclave setpoint and actual test temperature may have been different. Later testing exhibited a 650°C setpoint resulted in a sample temperature in the lower 600s °C. Complete temperature profiling for the autoclave system is provided in [Dunlevy, 2009].

2.3.7 Sample Characterization Methods

Before the initial placement into the autoclave, each sample was photo documented with a Nikon D80 camera with 60 mm lens and weighed with a Mettler Toledo XS105 DualRange Scale. The scale had a range and accuracy of 20.00001g ± .01 mg. Each sample was weighed until three consecutive attempts were within 0.02 mg. The surface morphology was examined with a Topcon ABT150S Scanning Electron Microscope (SEM). Prior to SEM examination, each sample was lightly coated in gold to provide conductivity in the SEM. The surface SEM analysis was focused on exploring any abnormal oxide growth, surface conditions, and unique corrosive behavior. Electron dispersive x-ray spectroscopy (EDX) was used to quantify the elemental composition.

After the surface of each sample was sufficiently characterized, each sample was sectioned in half using a LECO VC-50 diamond, slow-speed saw. One piece of the sample was returned to the desiccator for storage and further analysis, while the other half was mounted in Buehler Epoxicure. The sample was oriented such that the cross section and oxide thickness would be exposed after polishing. This was done to further characterize the oxide layer and any microstructural changes. Each mounted sample was wet polished with an Automet 3 Autopolisher by the following technique:

1. 180 grit sand paper, 120 rpm, 2 minutes, 3 lbs per sample

2. 240 grit sand paper, 120 rpm, 2 minutes, 3 lbs per sample
3. 400 grit sand paper, 120 rpm, 2 minutes, 2.5 lbs per sample
4. 800 grit sand paper, 120 rpm, 2 minutes, 2.5 lbs per sample
5. TexMet 1500 wheel with 3 micron MetalDi suspension, 120 rpm, 2 minutes
6. Rinsed in deionized water in ultrasonic cleaner for 2 minutes
7. ChemoMet wheel with MasterPrep 0.05 micron alumina suspension, 120 rpm, 2 lb per sample, 3 minutes.
8. Rinsed in deionized water using ultrasonic cleaner for 2 minutes

Lastly, each mounted sample was coated with gold prior to further SEM and EDX analyses.

2.4 Chapter Summary

Each alloy tested in this work was introduced and a brief description of properties and uses was provided. This chapter also covered the experimental procedure and provided a detailed description of the test apparatus and operation. The sample analyses included photo documentation, weight gain, surface SEM and EDS documentation, and cross-sectioned SEM and EDS analyses. Sample preparation for both the pre and post test work was discussed.

2.5 References

1. Klueh, R.L., Harries, D.R., "Development of high (7–12%) chromium martensitic steels. In: High-Chromium Ferritic and Martensitic Steels for Nuclear Applications", ASTM International, 2001.

2. Masuyama, F., "New developments in steels for power generation boilers, in: R. Viswanathan, J. Nutting (Eds.), Advanced Heat Resistant Steels for Power Generation", Conference Proceedings, San Sebastian, Spain, April 27–29, 1998.

3. Viswanathan, R. Bakker, W.T., "Materials for boilers in ultra supercritical power plants", in: Proceedings of 2000 International Joint Power Generation Conference (IJPGC2000-15049), Miami Beach, Florida, July 23–26, 2000.

4. Gupta, G., Was, G.S., Alexandreanu, B., "Grain boundary engineering of ferritic-martensitic alloy T91", Metallurgical and Materials Transactions A, Vol. 35, Number 2, February 2004.

5. World Wide Web: http://www3.interscience.wiley.com/cgi-bin/fulltext/119553209/PDFSTART, Accessed May 7, 2010.

6. ASTM Standard A240 – 10, "Standard Specification for Chromium and Chromium-Nickel Stainless Steel Plate, Sheet, and Strip for Pressure Vessels and for General Applications," ASTM International, West Conshohocken, PA, 2010.

7. ASTM Standard A182 – 98a, "Standard Specification for Forged or Rolled Alloy and Stainless Steel Pipe Flanges, Forged Fittings, and Valves and Parts for High-Temperature Service," ASTM International, West Conshohocken, PA, 1998.

8. Jones, D.A., *"Principles and Prevention of Corrosion, 2nd Ed."*, Prentice Hall, Upper Saddle River, NJ, 1996.

9. Jones, Chapter 15

10. World Wide Web: http://www.sandmeyersteel.com/316-316L.html, Accessed May 7, 2010

11. ASTM Standard A240 – 10, "Standard Specification for Chromium and Chromium-Nickel Stainless Steel Plate, Sheet, and Strip for Pressure Vessels and for General Applications," ASTM International, West Conshohocken, PA, 2010.

12. World Wide Web: http://www.rjsales.com/techdata/alloys/310s.html, Accessed May 7, 2010

13. ASTM Standard A182 – 09a, "Standard Specification for Forged or Rolled Alloy and Stainless Steel Pipe Flanges, Forged Fittings, and Valves and Parts for High-Temperature Service," ASTM International, West Conshohocken, PA, 2009.

14. World Wide Web: http://www.rjsales.com/techdata/alloys/al6xn.html, Accessed May 7, 2010.

15. ASTM Standard B676 – 03, 2009, "Standard Specification for UNS N08367 Welded Tube" ASTM International, West Conshohocken, PA, 2003.

16. World Wide Web: http://hpalloy.com/alloys/descriptions/INCOLOY800H.html, Accessed May 7, 2010.

17. World Wide Web: http://www.megamex.com/incoloy_800H_800HT.html, Accessed May 7, 2010.

18. World Wide Web: http://hpalloy.com/alloys/descriptions/INCOLOY800H.html, Accessed May 7, 2010.

19. World Wide Web: http://www.haynesintl.com/pdf/H3060.pdf, Accessed May 7, 2010

20. World Wide Web: http://www.haynesintl.com/pdf/h3073.pdf, Accessed May 7, 2010

21. World Wide Web: http://www.rjsales.com/techdata/alloys/a625.html, Accessed May 7, 2010

22. ASTM Standard B676 – 03, 2009, "Standard Specification for UNS N08367 Welded Tube" ASTM International, West Conshohocken, PA, 2003.

23. World Wide Web: http://www.suppliersonline.com/propertypages/NimonicPE16.asp, Accessed May 7, 2010

24. ASTM Standard B676 – 03, 2009, "Standard Specification for UNS N08367 Welded Tube" ASTM International, West Conshohocken, PA, 2003.

25. Madina, V., "Corrosion of Steels in CO2 Environments: Literature Review", Massachusetts Institute of Technology, June 2008.

26. Capdevila, C., et. al., "Grain Boundary Mobility in Fe-Base Oxide Dispersion Strengthened PM2000 Alloy", ISIJ International, Vol. 43 (2003), No. 5, pp. 777-783.

27. Dunlevy, M.W., "An Exploration of the Effect of Temperature on Different Alloys in a Supercritical Carbon Dioxide Environment", Master's Thesis, Massachusetts Institute of Technology, September 2009.

28. World Wide Web: http://www.scifun.org/chemweek/pdf/CarbonDioxide.pdf, Accessed May 13, 2010.

Chapter 3 – Results and Discussion - Alloy Performance Characterization

3.1 Introduction

The characterization of each alloy consisted of surface documentation, both with photo documentation and surface SEM analyses; weight gain analysis, and sub surface oxide analysis. All of these analyses contribute to the overall understanding of the alloy performance in the S-CO_2 environment and poor performance in any one aspect of the corrosion behavior can disqualify a particular alloy. The surface oxide characterization serves to document the outer surface of each alloy, namely to determine if the outer oxide layer is susceptible to pitting, film rupture, or other localized failure methods. The weight gain analysis documents the rate of oxide growth by measuring the weight gain or loss. Alloys experiencing high weight gain rates are undesirable because it is an indication the outer oxide is porous and the oxygen anions are able to readily react with the metal ions, which can ultimately result in surface metal consumption. Lastly, the sub-surface oxide analyses takes a closer look at the structure and composition of the cross-section of each alloy and any oxide that may have formed along with investigating any effects on the base metal, such as preferential formation sites. The test matrix for the corrosion tests and alloys studies in this work is presented in Table 3-1. Every alloy was tested up to 3000 hours, in 500 hour increments, but only selected alloys within the 3000 hour sample set are discussed in this chapter.

Table 3-1: Test Matrix

Alloy	Temperature (°C)	Pressure (MPa)	Exposure Time (hours)
F91	610	20	3000
HCM12A	610	20	3000
PM2000	610	20	3000
316SS	610	20	3000
310SS	610	20	3000
AL-6XN	610	20	3000
800H	610	20	3000
625	610	20	3000
Haynes 230	610	20	3000
PE-16	610	20	3000

3.2Oxide Surface Characterization

3.2.1 General

Each tested alloy was both photo documented and then characterized using scanning electron microscopy (SEM) to further classify the oxide surface. Each alloy is discussed here, but several are discussed in further detail as they warrant closer attention and discussion.

The photo documentation of all the 3000 hour samples is provided in Figure 3.1. The photo documentation shows notable behavior from several alloys, namely F91 and HCM12A, while other alloys appear to undergo normal high temperature, stable oxidation. Alloy F91 experienced severe oxide spallation: The dark areas of the image are the spalling oxide and the lighter areas are freshly forming oxide. Alloy HCM12A experienced preferential oxide nucleation and growth from regions of high stress. The spacing of the oxide corresponds to the grit spacing of the final surface finish step, which was polishing with 400 grit sand paper. It should be noted here that a 400 grit surface finish is common in industrial applications and reflects the true surface behavior. Alloys 316SS and 310SS experienced sporadic and localized oxide growth, with 310SS being more sparse than 316SS.

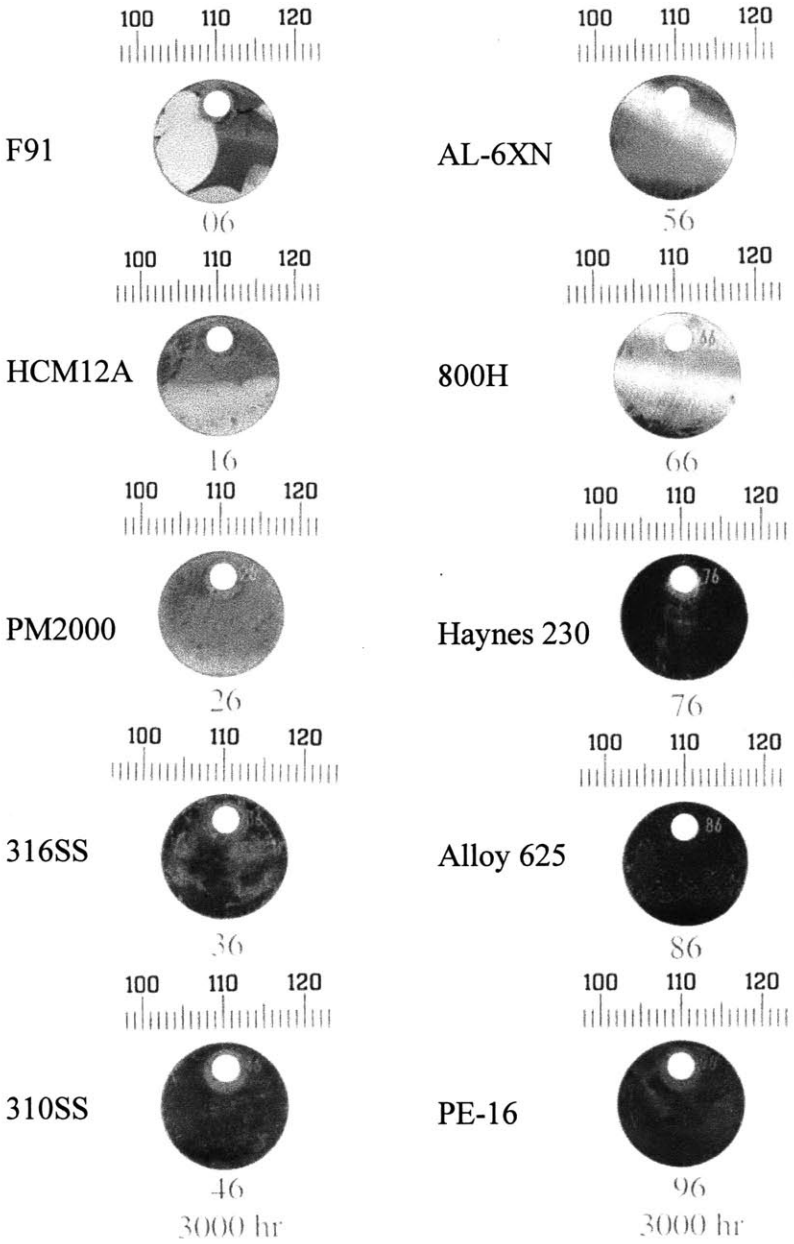

Figure 3.1: Photo documentation of 3000 hour samples

3.2.2 Specific Analysis

Alloys F91, HCM12A, PM2000, 316SS, and 310SS are presented here with surface SEM micrographs. The remaining alloys exhibited minimally visible oxide films on the surface with few noteworthy features. The SEM surface analysis for the alloys not presented and discussed in this section and are presented in the appendix. The SEM micrograph in Figure 3.2 shows both the surface of Alloy F91 at an oxide rupture location and focused solely on the base layer, which shows an even oxide growth. The

oxide growth of Alloy HCM12A is shown in Figure 3.3. The arrow in Figure 3.3A indicates the polishing direction. Figure 3.3B is a higher magnification micrograph of the oxide growth and shows thick growth along the polishing band and sparse oxide growth in between the bands. The surface of Alloy PM2000 exhibits minimal visible oxide growth on the surface. Figure 3.4 shows localized oxide surface irregularities are present and may be attributed to the surface roughness of the test coupon. The arrow in Figure 3.4 indicates the polishing direction.

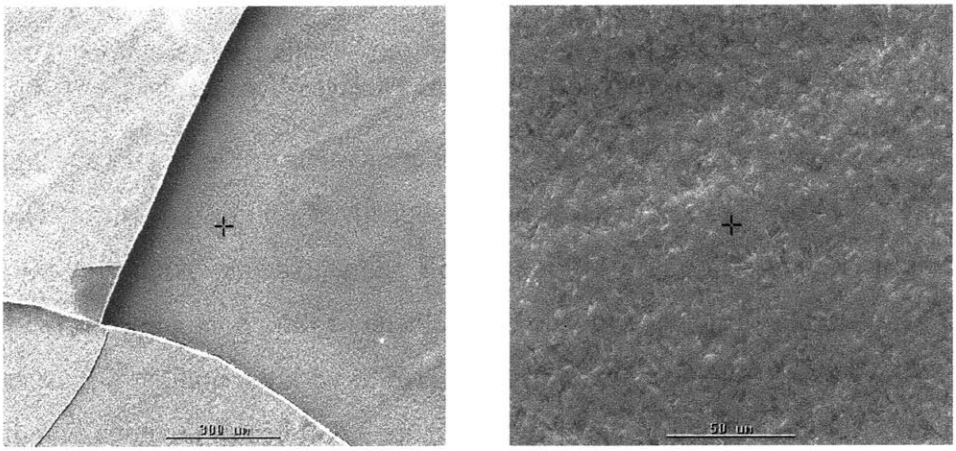

A – 75x magnification B – 500x magnification

Figure 3.2 Alloy F91 SEM Surface Micrographs

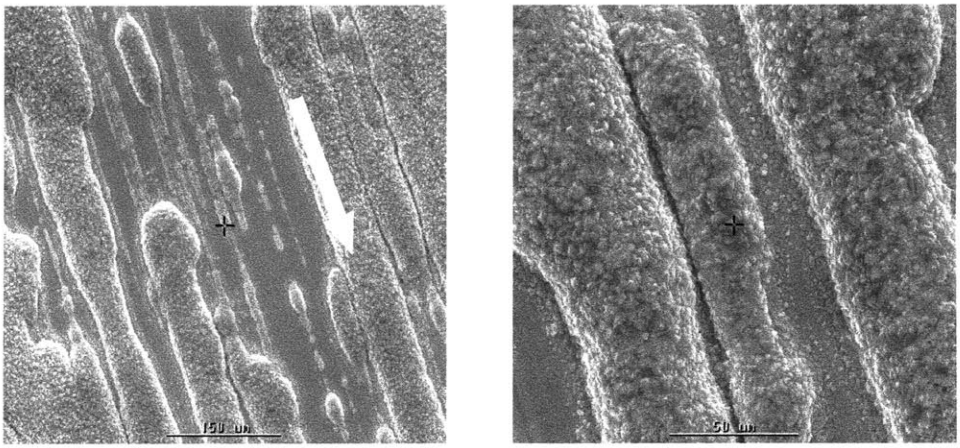

A – 75x magnification B – 500x magnification

Figure 3.3: Alloy HCM12A SEM Surface Micrographs

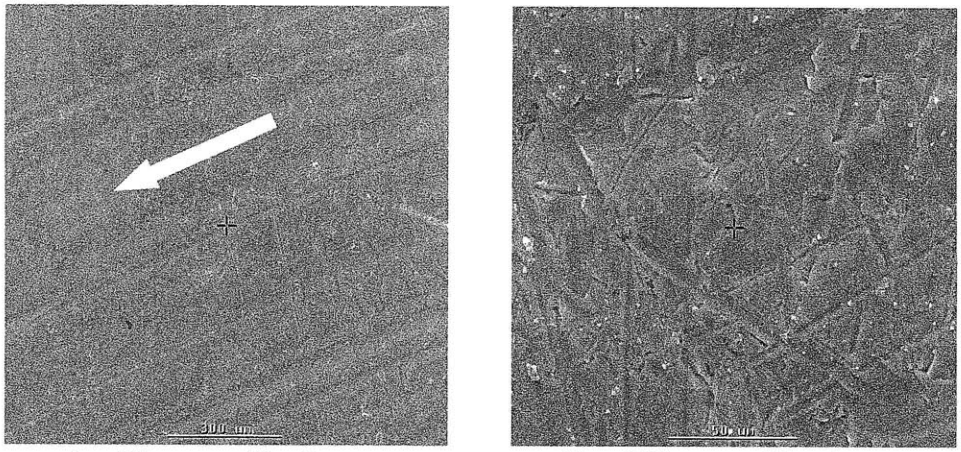

A – 75x magnification B – 500x magnification

Figure 3.4: Alloy PM2000 SEM Surface Micrographs

The oxide growth on Alloys 316SS and 310SS are shown in Figure 3.5 and Figure 3.6, respectively. Alloy 316 exhibits areas of localized oxide growth. The higher magnification view of Alloy 316 in Figure 3.5B shows that the oxide growth occurs in clusters of finger-shaped oxide. Outside these clusters a thin, homogeneous oxide film is present. Alloy 310SS behaves very similar to 316SS, with the notable differences being fewer clusters of oxide growth. The arrow in Figure 3.6 indicates the polishing direction.

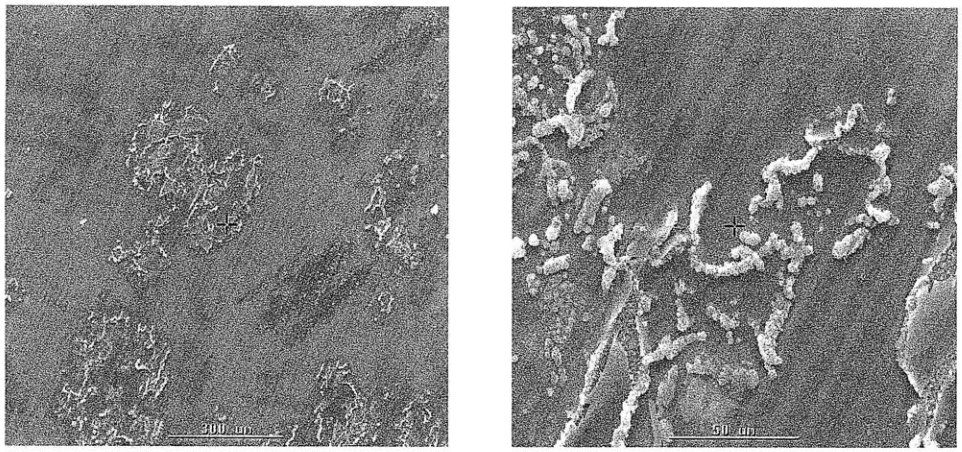

A – 75x magnification B – 500x magnification

Figure 3.5: Alloy 316SS SEM Surface Micrographs

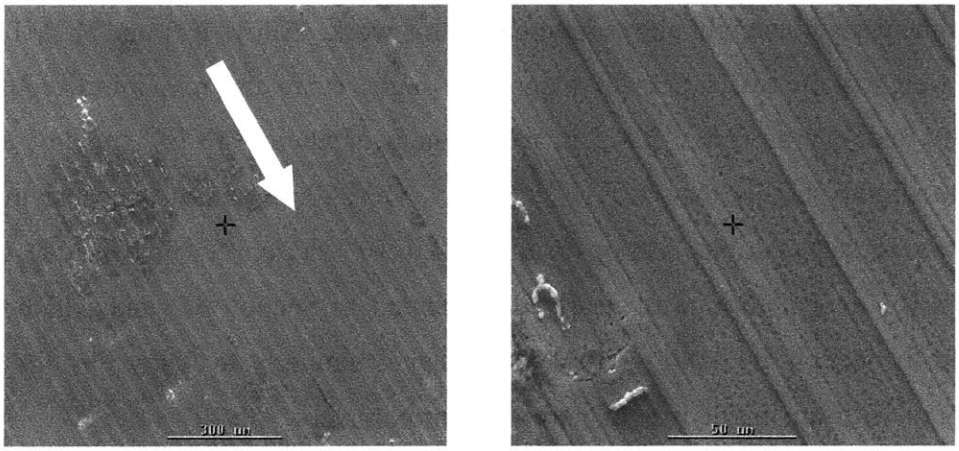

A – 75x magnification B – 500x magnification

Figure 3.6: Alloy 310SS SEM Surface Micrographs

3.3 Weight Gain Analysis

Each test coupon was weighed before testing and then at each subsequent 500 hour interval when the test was stopped. This served to measure the weight gain of each alloy to further determine potential alloys for use in S-CO_2. If an alloy were to exhibit excessive weight gain it would indicate that the metal oxidizes readily in the CO_2 atmosphere. Ideal performance would consist of thin, protective oxide growth that follows parabolic behavior with slow growth rate in the approximately linear region with no break away behavior.

All but two of the alloys tested in this work exhibited good weight gain characteristics. The weight gain data is presented in two ways to facilitate understanding of the ongoing processes. First, the cumulative weight gain per area is presented in Figure 3.7. This unit of weight gain was chosen because it eliminates the dependency on surface area size. However, the disadvantage of this form of presentation is that localized high corrosion rates can be "blended" down and appear to be much slower than it really is. Figure 3.7 is provided to focus on the total or cumulative weight gain per area, not on the rate of weight gain or loss, or the incremental weight gain per time step. The incremental weight gain is the difference between time steps. The notable features of this graph are primarily in two categories; those alloys with high weight gain and those with minimal weight change. In the first category are alloys F91 and HCM12A and the second category

contains the remaining eight alloys reported in this work. Alloys F91 and HCM12A have exhibit weight gain two orders of magnitude higher than the remaining eight alloys. Alloy F91 exhibits an initial jump in weight gain of about $3.6x10^{-3}$ mg/cm^2 and then climbs to slightly higher than $5.0x10^{-3}$ mg/cm^2 over 2500 hours of exposure to S-CO_2. The last time step exhibits a drop to about $4.0x10^{-3}$ mg/cm^2, which is due to oxide spallation. The spallation was clearly documented in Section 3.2 and will be further discussed in Section 3.4. Alloy HCM12A behaves similarly to Alloy F91 for the first 2500 hours with an initial weight gain of approximately $3.0x10^{-3}$ mg/cm^2. However, unlike Alloy F91, Alloy HCM12A continues to gain weight after 2500 hours and climbs to a total weight gain of approximately $5.5x10^{-3}$ mg/cm^2 after 3000 hours.

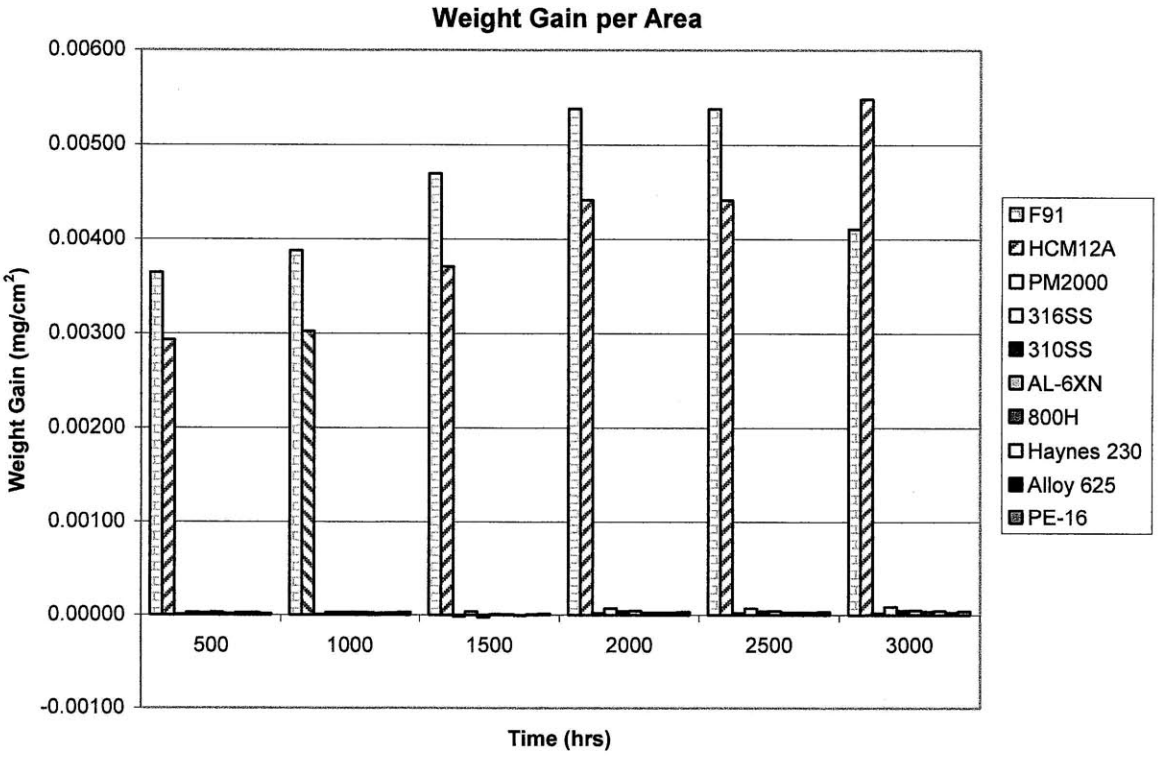

Figure 3.7: Cumulative weight gain per area[1]

Figure 3.8 shows the same data as in Figure 3.7, but with Alloys F91 and HCM12A removed to allow the trends of the remaining alloy weight gain data to be clearer. All of the alloys, exhibit an initial step change in weight between time zero and 500 hours. This

[1] Note, the alloys in key from top to bottom are given in same order from left to right on graph

is due to the initial reaction with the base material and formation of an oxide layer. Alloy PM2000 exhibits the smallest initial weight gain at the 500 hour mark ($7.4x10^{-6}$ mg/cm^2) and very minimal weight gain over the 3000 hours in the autoclave. The remaining alloys exhibit an initial weight gain around $2.0x10^{-5}$ mg/cm^2 and end with weight gains around $4.0x10^{-5}$ mg/cm^2. Alloy 316 begins with similar weight gain, but ends the test with a cumulative weight gain notably higher than the alloys presented in Figure 3.8 at slightly higher than $8.0x10^{-4}$ mg/cm^2. The amount of weight gained by Alloy 316SS is moderate enough to not be considered breakaway oxide growth. Nearly every alloy exhibited continual oxide weight gain over the duration of the test. Only Alloy F91 was an exception to this trend. This can be explained with the oxide spallation evident in the photo documentation and surface SEM analysis. The total weight gain per area for each alloy, measured at 3000 hours, is recorded in Table 3-2. One additional notable feature to the weight gain data presented here is that the majority of the alloys exhibited a weight loss between 1000 and 1500 hours, but the only sample showing any form of visible weight loss in this experiment was Alloy F91. One additional feature in the weight gain data is that seven of the ten alloys in this work had their minimum weight gain occur at the same measurement window (1500 hours). The sub-surface oxide analysis did not reveal any additional reasons for this the sudden weight drop between hours 1000 and 1500 and then weight gain between hours 1500 and 2000. This may be an experimental error because no explanation can be offered at this point to these losses. The data recorded at 2000 hours further hint at a possible measuring error at 1500 hours based on an almost predicable trend from the first two and last three measurement points. Not focusing on the 1500 hour window, each alloy, excluding Alloy F91, exhibits continual weight gain (weight per area) for the full experimental window.

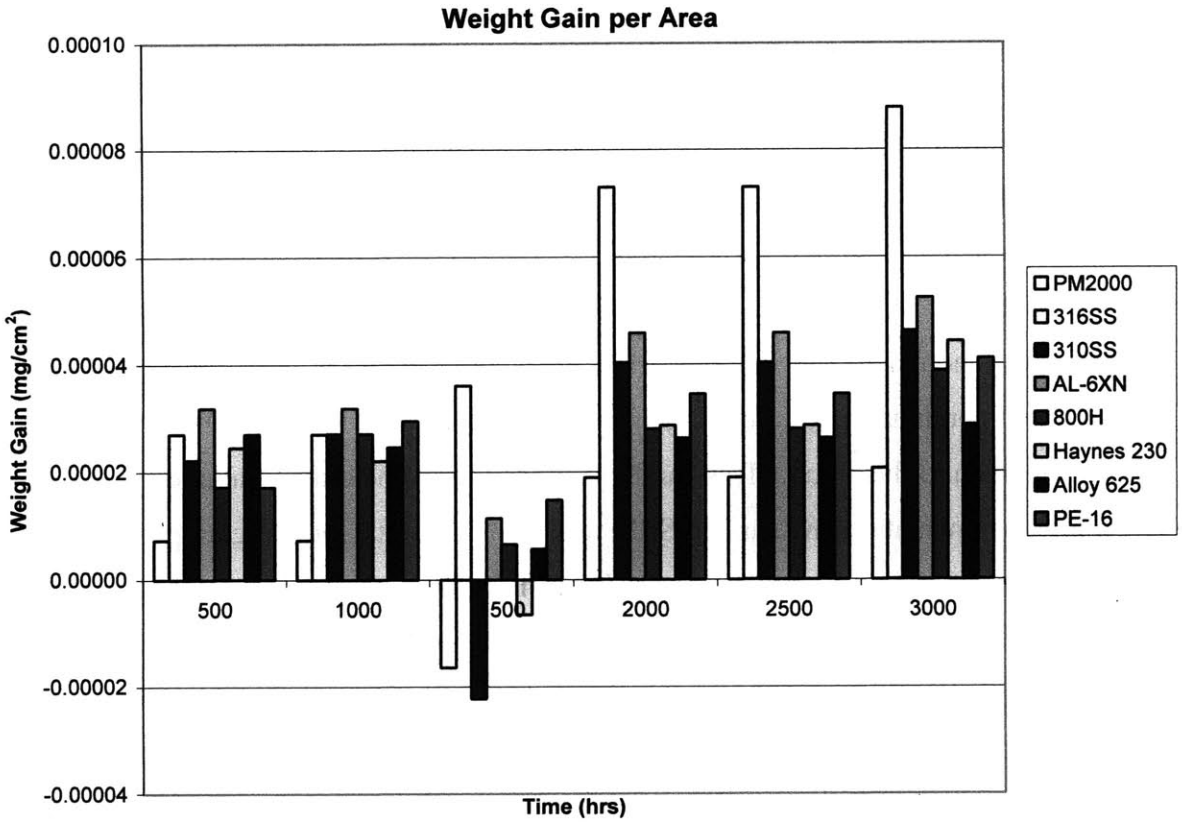

Figure 3.8: Weight gain per area, Alloys F91 and HCM12A not present

Table 3-2: 3000 hr weight gain

Alloy	**Weight gain at 3000 hours** (mg/cm^2)
F91	$4.1x10^{-3}$
HCM12A	$5.5x10^{-3}$
PM2000	$2.1x10^{-5}$
316SS	$8.7x10^{-5}$
310SS	$4.6x10^{-5}$
AL-6XN	$5.2x10^{-5}$
800H	$3.9x10^{-5}$
Haynes 230	$4.4x10^{-5}$
Alloy 625	$2.9x10^{-5}$
PE-16	$4.1x10^{-5}$

The weight gain behavior can be further analyzed by taking a closer look at the weight gain rate. This was calculated by determining the total weight gain for each time increment and dividing the gain by the exposure time. Corrosion weight gains are

typically recorded in mg/area*day or mg/area*year. The weight gain rate in this work is presented in mg/cm^2day. These results are divided into two groups: The first is alloys with high rates of weight gain and the second are the alloys within minimal rates of weight gain. The first category contains Alloy F91 and HCM12A. Alloy F91 experienced the highest weight gain rate with an initial rate of nearly 0.18 mg/cm^2day and settling down to a final rate of 0.032 mg/cm^2day at 3000 hours. Similarly, Alloy HCM12A exhibits an initial weight gain rate of approximately 0.14 mg/cm^2day and slows to about 0.043 mg/cm^2day at 3000 hours. The behavior of these two alloys is common in many engineering alloys and is referred to as parabolic weight gain. The initial rate is high because the fresh metal is readily oxidized do to the availability of metal ions. As the oxide layer is formed the weight increases (Figure 3.7), but the rate decreases due to the decreasing rate of diffusion of both the oxygen anions and metal ions (Figure 3.9).

Figure 3.10 is the same as Figure 3.9, but with Alloys F91 and MCM12A removed to enable a closer look at the remaining alloys. Each of the remaining seven alloys all exhibit a high initial weight gain rate, but reduces with increasing exposure time. Alloy AL-6XN has the highest rate gain in the second group of alloys with a rate slightly higher than $1.5x10^{-3}$ mg/cm^2day and reducing to slightly less than $5.0\ x10^{-4}$ mg/cm^2day. Alloy PM2000 exhibits the lowest weight gain rate of all the alloys in this work and begins with a rate of approximately $3.6x10^{-4}mg/cm^2day$ and ends with a rate of $1.7x10^{-4}$ mg/cm^2day. Alloys PM2000, 310SS, AL-6XN, 800H, Haynes 230, and PE-16 exhibit the lowest weight gain rate at 1500 hours, which stems from the lower recorded weights at that time point, as evident in Figure 3.8. There was no documented spallation or other explainable form of weight loss for these alloys at 1500 hours.

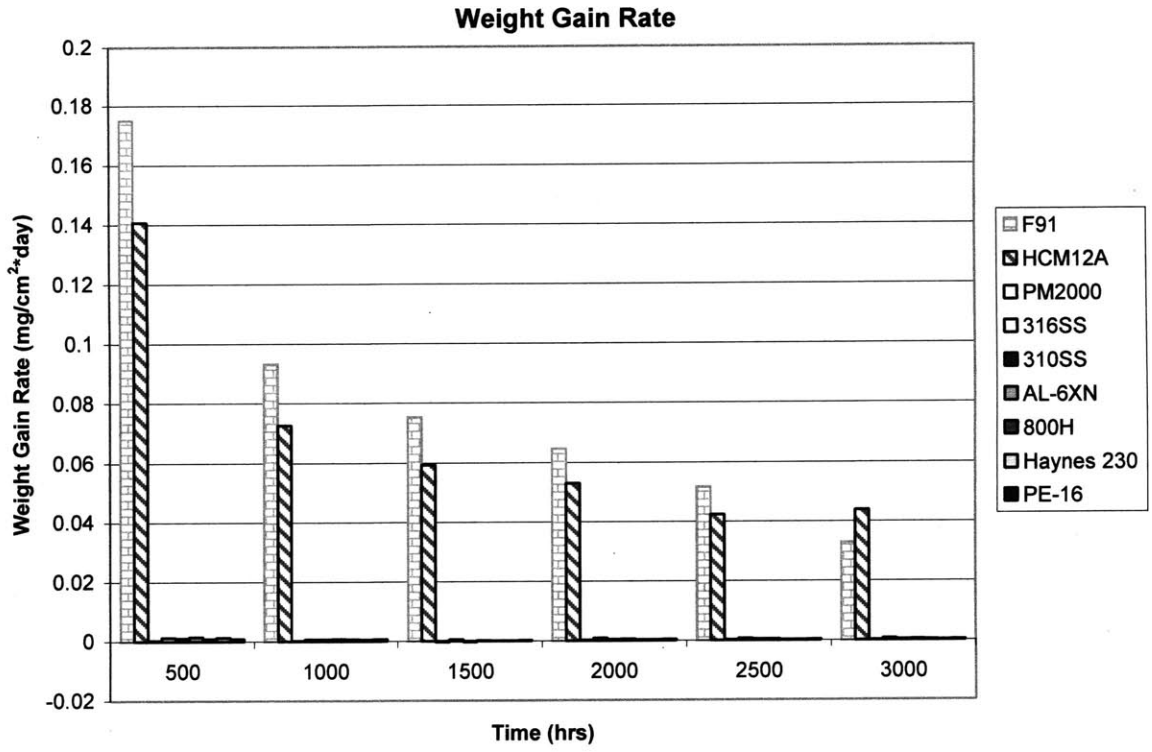

Figure 3.9: Weight gain rate of all tested alloys

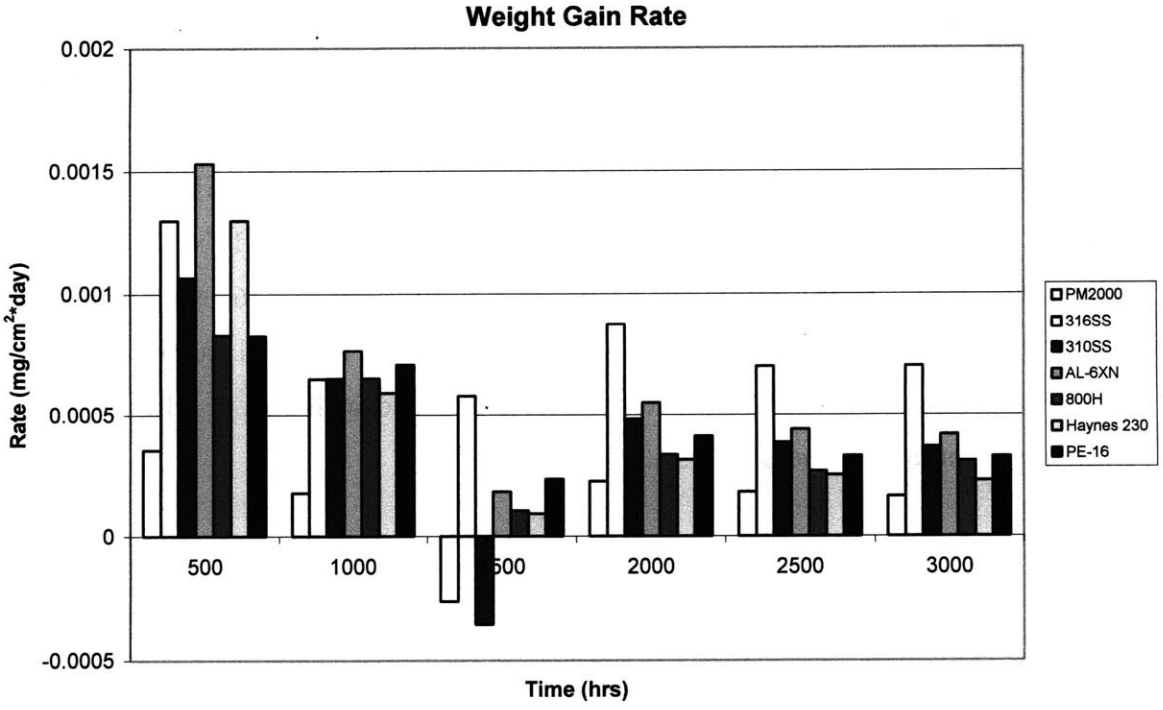

Figure 3.10: Weight Gain Rate of tested alloys, except Alloys F91 and HCM12A

3.4 Cross Section Oxide Characterization

Characterization of the effect of S-CO_2 on the alloys in this work required the oxide layer (if present) to be examined for composition, behavior, and further behavior. The cross sectional analysis enables further characterization methods to be employed, such as measuring the oxide thickness and elemental analysis and composition as a function of position. The samples for the cross sectional analysis were prepared by sectioning, epoxy mounting, and polishing each sample in a plane orthogonal to its oxide growth. Furthermore, each mounted sample was coated in gold and grounded with copper adhesive to facilitate charge dissipation in the SEM. This sample mounting arrangement is illustrated in Figure 3.11. The alloy shown in Figure 3.11 is Alloy HCM12A, which will be discussed in further detail in this chapter. Every sample was examined in this manner, but only for a discreet set of time points: The most important being the samples exposed to S-CO_2 for 3000 hours. Intermittent time points were examined for specific alloys, mainly those being the samples with oxide growth or other behavior in need of further examination.

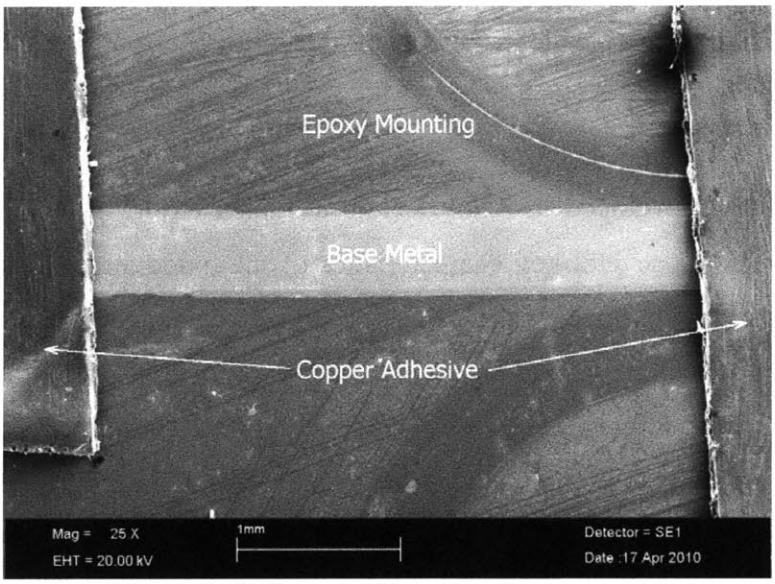

Figure 3.11: Sample Mounting Arrangement

The results for alloys F91, HCM12A, PM2000, 310SS, and 625 are presented in this chapter because they provide the best examples of pertinent discussion points in this work. Oxide cracking and spallation was observed in Alloys F91 and HCM12A. The

cracking likely resulted form thermal expansion mismatch between the oxide and alloy. Upon cooling, the tensile stresses generated in the thick oxide layers were sufficient to cause microcracking, ultimately leading to agglomeration of cracks and oxide spallation. Those alloys not explicitly covered in this chapter are documented in the appendix with complete sets of SEM images and data.

3.4.1 Alloy F91

Figure 3.12 and Figure 3.13 show the electron micrographs and elemental maps, respectively, for Alloy F91. This alloy exhibited poor exposure characteristics in S-CO_2. The oxide growth was rapid, but unstable and ultimately ended in spallation, as evident in Figure 3.12. This was first identified on the surface of the alloy in the photo documentation. The oxide spallation also explains the weight loss between hours 2500 and 3000, which was discussed in Section 3.3. The SEM analysis clearly showed the oxide flakes in both the surface and cross sectional analyses. However, the surface analysis shows a higher degree of spallation than the cross sectional analysis because additional oxide was lost during the cross sectional cutting process. However, the high weight gain and unstable oxide behavior of this alloy disqualifies it as a potential candidate for use in S-CO_2 systems.

The unstable oxide developed in Alloy F91 is a duplex oxide. Elemental maps were generated to elucidate several key characteristics of the oxide and are shown in Figure 3.13. The maps include three images; the first image is one of the base metal and the detaching oxide layer. The second image is a map of iron and the third image is a map of chromium. The iron map exhibits an enrichment of iron in approximately the outer 50% of the detaching oxide. Chromium shows enrichment in the inner 50% of the oxide and slight depletion on the outer region of the base metal. Based on the thermodynamics of the iron-oxygen phase diagram, the outer layer is wustite phase and the inner layer is an iron-chromium spinel, common in Alloy F91. To confirm the phases it is necessary to use an x-ray analysis and/or x-ray photoelectron spectroscopy (XPS), which was not employed in this work.

It is important to note here that the nominal composition of Alloy F91 is 8-9.5 wt% chromium, which is considered a low-chromium steel. The outer layer becomes chromium depleted and forms wustite phase and the inner layer forms an iron-chromium spinel. The wustite phase spalls off leaving the spinel as the primary oxide. This alloy can be improved for the use in the S-CO_2 environment if the chromium content was increased. However, based on the overall performance of this alloy, it is recommended that other potential candidate alloys be explored.

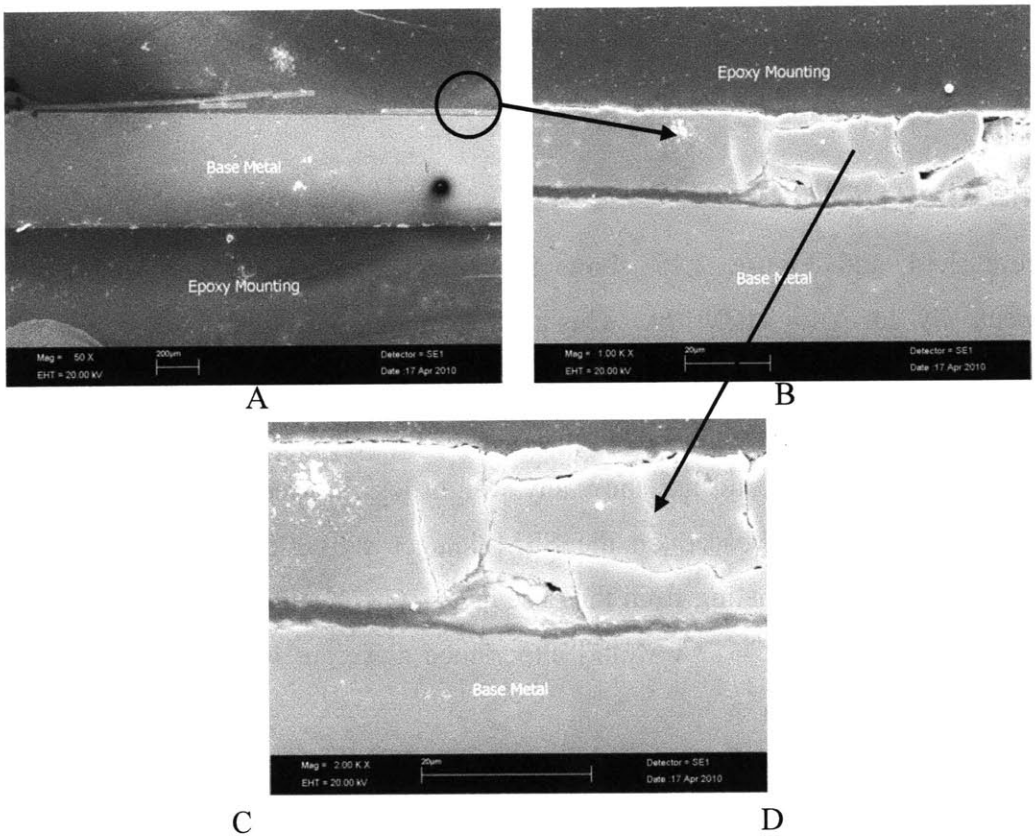

Figure 3.12: SEM Micrographs of Alloy F91

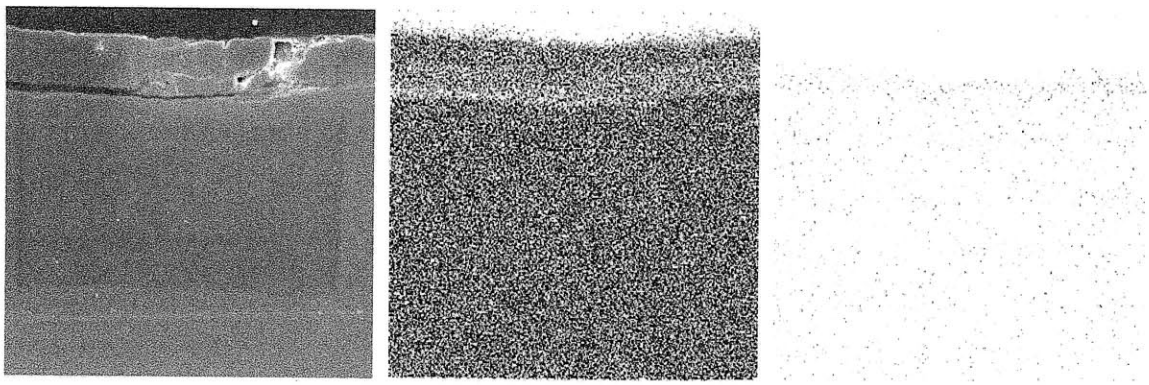

Alloy at 500X Iron EDX Map Chromium EDX Map

Figure 3.13: Iron and Chromium Maps of Alloy F91

3.4.2 Alloy HCM12A

Figure 3.14 and Figure 3.15 show the SEM micrographs and elemental maps, respectively, for Alloy HCM12A. This alloy exhibited poor qualities over the 3000 hour age time in S-CO_2. The oxide layer is porous, unstable, and cracks and spalls away from the base material. The weight gain analysis for this alloy showed that the weight gain rate was very high, but did not show any weight loss between time steps, as seen with Alloy F91. However, based on the SEM images it is clear that the oxide layer is fragmented and delaminating from the base layer. Given additional age time in S-CO_2 it is likely that Alloy HCM12A would experience a weight loss when the oxide flakes away.

Figure 3.14A shows a low magnification view of the cross section of Alloy HCM12A. The important feature to point out is the irregular and rough oxide layer. Although only partial and no full sections are missing, the protective qualities of the oxide are highly diminished and spallation is likely to occur if the specimens are aged longer than 3000 hours. Figure 3.14B is a close-up view of the black circle in Figure 3.14A. The porosity and cracking oxide are clear at 500x magnification. The section of oxide highlighted in Figure 3.14B indicates that this particular section is cracked horizontally and vertically and given additional age time may flake off. Figure 3.14B also shows that only the outermost layer of oxide is spalling away from the base metal and a secondary base layer is present. The outermost layer is approximately 20 μm thick and the inner layer is

approximately 15 μm. Figure 3.14C clearly shows the degree of porosity of the outer oxide layer. Furthermore, the vertical crack extends into the secondary oxide layer causing further weakening and facilitating future flaking. It is also possible that the cracking may be due to the sample preparation method when it was mounted and polished in epoxy due to the oxide thickness.

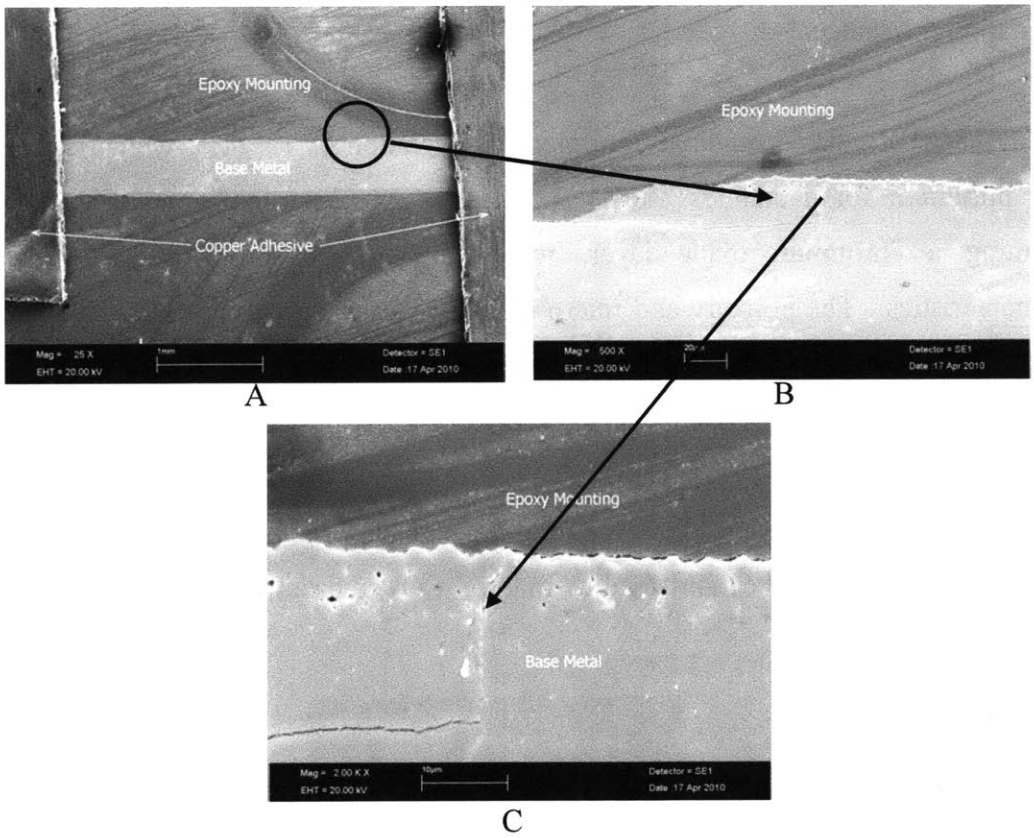

Figure 3.14: SEM Micrographs of HCM12A Oxide Layer

The elemental maps on Alloy HCM12A clearly indicate a duplex oxide layer and are shown in Figure 3.15. Similar to Alloy F91, iron is enriched in the outside oxide layer with chromium depletion. Chromium is enriched on the inner layer with iron depletion. This pattern of diffusion is common with the wustite-spinel duplex oxide also seen in Alloy F91. The outer layer is also slightly depleted of silicon and tungsten, while the inner layer has a homogeneous concentration comparable with the base metal. The silicon is alloyed with the HCM12A to improve oxidation resistance as it acts like chromium to prevent high temperature degradation. Silicon diffusion out of the outer

oxide increases the oxidation susceptibility, which is evident in the oxidation on the surface. However, the inner oxide layer, which is the layer beneath the porous micro cracking can be enhanced by the presence of the silicon. The slight tungsten depletion in the outer oxide layer is of little significance, if not a benefit. Tungsten is alloyed with HCM12A for the same reason as molybdenum, which is to improve high temperature strength and creep resistance, but at the expense of being detrimental high temperature oxidation resistance.

Alloy HCM12A has a nominal chromium composition of 12 wt%, which is considered the minimum for a stainless steel. Increasing the chromium content will facilitate forming a chromium oxide layer, which is known for its desirable protective characteristics. The porosity and micro cracking in the outer oxide layer is undesirable and will contribute to base metal loss as it eventually spalls away from the sample. The weak outer oxide layer may have cracked and begun spalling upon sample cool down due to the differential expansion between the base metal and the oxide. Regardless, the weak oxide is highly undesirable and does not warrant any further consideration for Alloy HCM12A as a potential candidate alloy in the S-CO_2 environment.

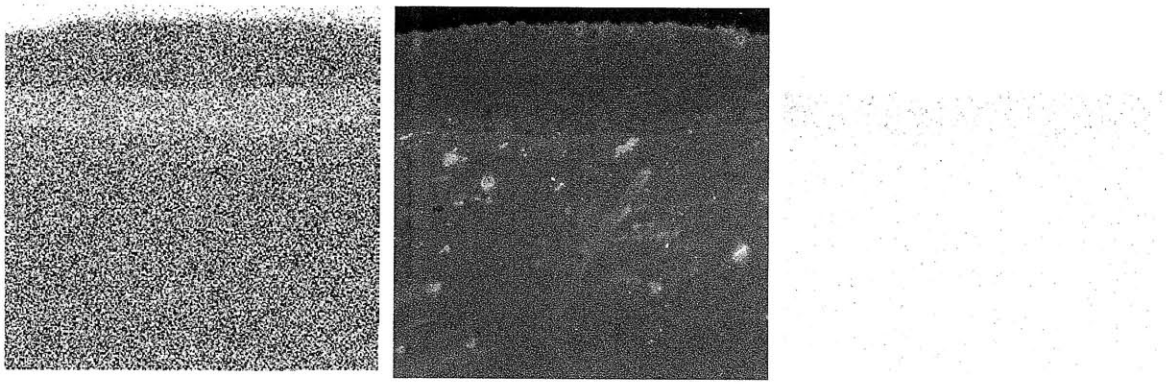

Iron EDX Map Alloy at 500X Chromium EDX Map

Figure 3.15: Iron and chromium elemental maps

3.4.3 Alloy PM2000

Figure 3.16 and Figure 3.17 show the SEM micrographs and elemental maps, respectively, for Alloy PM2000. This alloy performed well in the S-CO_2 environment, but there are several minor features that deserve discussion. The oxide layer is about 1 μm thick, stable, and overall, is well bonded to the base metal. The oxide layer does have some irregularity, such as surface roughness and minor flaking. The surface roughness is irregular and has a mean height of about 5 μm, which is evident in Figure 3.16. The small, dense oxide layer is most visible in Figure 3.16A and B and the localized flaking is shown in Figure 3.16C.

Elemental maps were produced for iron, chromium, aluminum, yttrium, and titanium to further characterize any potential enrichment or depletion of a given constituent. Maps of chromium and iron are provided in Figure 3.17 along with a scanning electron micrograph at 500X magnification. The elemental maps indicate no enrichment or depletion of iron or chromium, which are the most common elements in Alloy PM2000. Moreover, the elemental maps showed a homogeneous distribution of aluminum, titanium, and yttrium. Point EDX scans were also conducted on this alloy confirmed no elemental segregation. The flake pictured in Figure 3.16C and Figure 3.17 has the same nominal composition as the base metal and is not an unstable oxide formation. It should be noted that the flake in Figure 3.16 and Figure 3.17 may be due to the original surface roughness of the as-received alloy coupons and may not be an oxide stability issue. The surface roughness is documented in Figure 3.4and discussed further in Section 3.2. Overall, the oxide layer holds up well and exhibits desirable protective characteristics.

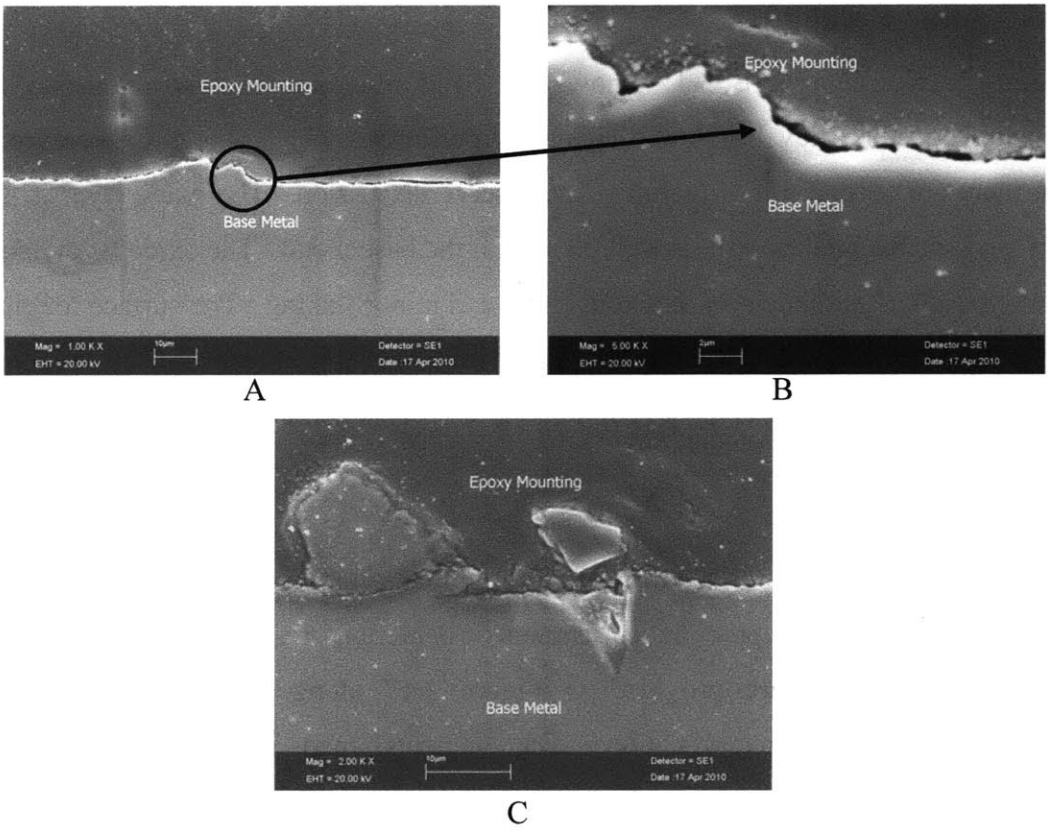

A B C

Figure 3.16: SEM Micrographs of Alloy PM2000

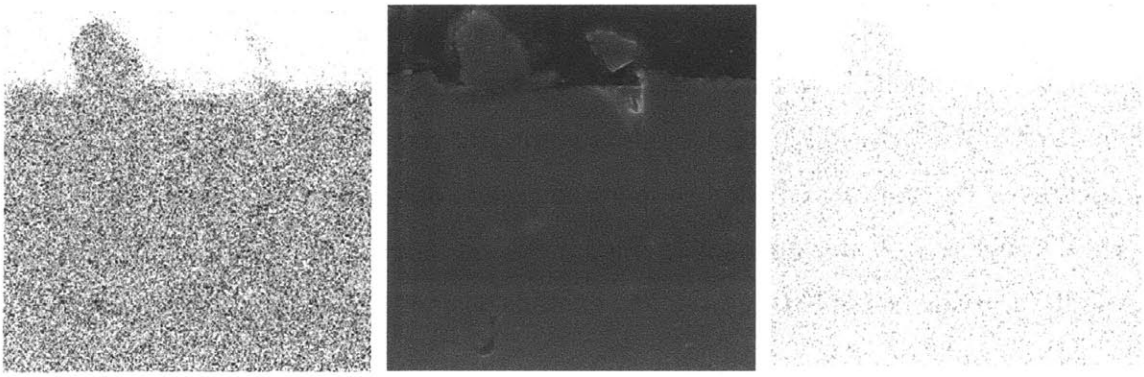

Iron EDX Map Alloy at 500X Chromium EDX Map

Figure 3.17: Elemental maps of iron and chromium on Alloy PM2000

3.4.4 Alloy 310SS

Figure 3.18 and Figure 3.19 show the electron micrographs and elemental maps, respectively, for Alloy 310SS. This alloy performed well in the S-CO_2 environment: It formed a narrow, dense oxide layer and exhibited little weight gain. This alloy is

discussed here to highlight several features. Figure 3.18A shows delamination of the epoxy mounting from the sample. Figure 3.18B shows a higher magnification view of the delamination, but more importantly, shows the thin, dense, protective oxide. The lighter areas of color within the base material in Figure 3.18C are not features of the base metal, but remnants of the final polishing step in sample preparation, which employed 0.05 μm dispersed alumina. These areas are also clearly present over other areas of the epoxy mounting and specimen and are also present in Figure 3.18A. Although the oxide layer appears ideal in Figure 3.18B, Figure 3.18D shows areas of porosity. It appears as if the epoxy mounting is beginning to detach from the sample, which may contribute to the porosity appearance. Moreover, this porosity may be remnants of the finger-like, sporadic surface oxide present in Figure 3.6.

Elemental maps were generated to further characterize any compositional changes evident in Alloy 310SS. These maps were generated for iron, chromium, and nickel, which are the predominant constituents in this alloy. No depletion or enrichment was noticeable in any of these three elements. Alloy 310SS is considered a high chromium stainless steel because it nominally contains 24-26 wt% chromium. Alloy 310SS also has a nominal nickel content of 19-22 wt%. High amounts of both chromium and nickel are the predominant reason Alloy 310SS performed so well in the S-CO_2 environment. High amounts of chromium and nickel are added to this series of alloy to improve oxidation resistance, especially at high temperature.

Overall, Alloy 310SS performed well in the S-CO_2 environment and warrants further characterization and testing.

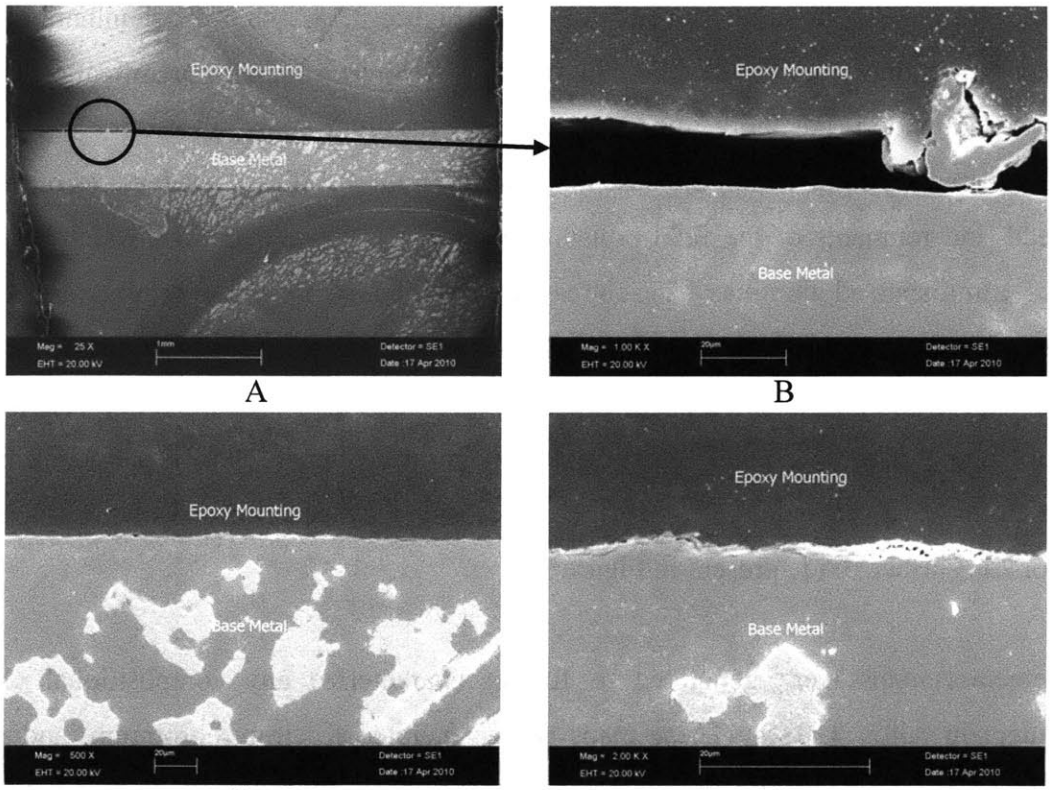

Figure 3.18: SEM Micrographs of Alloy 310SS

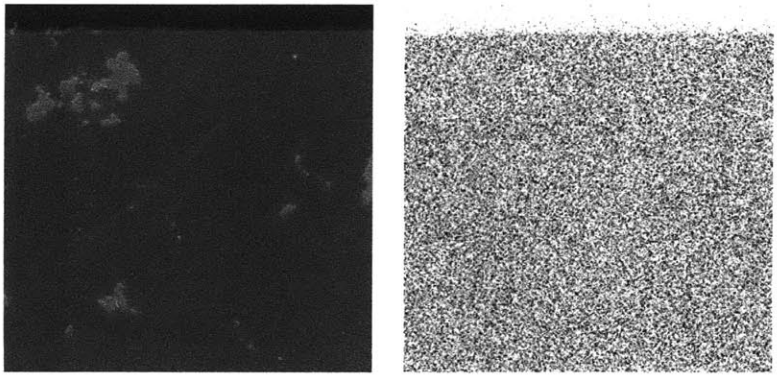

Alloy at 500X | Iron EDX Map

Chromium EDX Map | Nickel EDX Map

Figure 3.19: Iron, Chromium, and Nickel Elemental Maps

3.4.5 Alloy 625

Figure 3.20 shows the electron micrographs of Alloy 625. This alloy is briefly discussed here to provide an example of an alloy that has performed exceptionally well in the S-CO_2 environment and warrants further feasibility testing. The SEM micrographs are provided in Figure 3.20 and show that the oxide film on this alloy is a thin, dense, protective layer less than 1 μm thick. Elemental maps were constructed for Alloy 625 to further document any additional compositional changes. The maps are not recorded in this work because, similar to Alloy 310SS, no compositional changes occurred. The base metal exhibited a homogeneous distribution of iron, nickel, and chromium which are the three predominant elements. Alloy 625 is a nickel-based, high chromium, austenitic alloy. The high chromium content (>20 wt%), combined with the nickel-base, enables this alloy to develop high oxidation resistance.

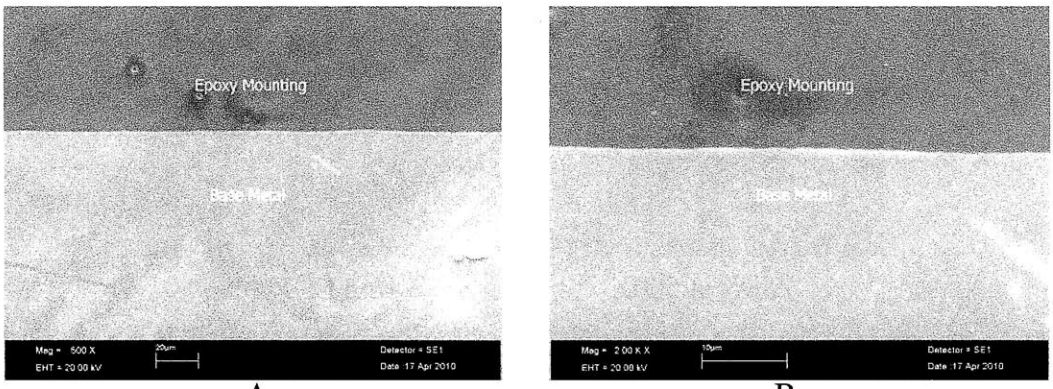

A B

Figure 3.20: SEM Micrographs of Alloy 625

3.5 Summary and Conclusions

The characterization of each alloy was broken into photo documentation, surface SEM analyses, weight gain, and sub-surface oxide analyses. The surface characterization with the SEM analysis revealed interesting characteristics for several alloys. Alloy F91 undergoes substantial weight gain and has very poor oxide characteristics: The oxide is a duplex type oxide and is porous, unstable, and readily undergoes spallation. Overall, Alloy F91 is unsuitable for use in S-CO_2 environments. The surface SEM analysis of alloy HCM12A revealed that the oxide layer is readily formed on the areas of higher stress, which was indicated by the oxide preferentially growing on the bands created by the 400 grit sand paper. Alloy HCM12A was susceptible to a high degree of weight gain and poor oxide characteristics such as porosity and spallation. Alloy HCM12A also formed a duplex oxide with an iron-rich outer layer and a chromium-rich inner layer. Alloy PM2000 exhibited stable behavior in the S-CO_2 environment. This alloy had the lowest weight gain of all the alloys covered in this work and no surface irregularities. Furthermore, Alloy PM2000 developed a thin, stable oxide layer, but did exhibit minor localized oxide spallation, but may be prevented with better initial surface preparation.

Only alloys F91 and HCM12A performed poor in the weight gain analysis. The remaining alloys all exhibited desirable weight gain characteristics; namely, a low weight

gain rate with no sudden weight oscillations, which could be an indication of oxide spallation.

Alloy 625 performed exceptionally in each category. This alloy exhibited no surface irregularities, minor weight gain, and a thin, stable oxide layer.

Chapter 4 - Summary, Conclusions, and Recommendations for Future Work

4.1 Summary and Conclusions

4.1.1 Overview

Ten alloys were corrosion tested for times up to 3000 hours in a S-CO_2 environment at 610°C and 20 MPa. This purpose of the experimental work was to determine which alloys are potential candidates for deployment in S-CO_2 cooled nuclear reactors. The alloys that performed well in these tests will undergo further testing and those that performed poorly will be disqualified from future work. The ten alloys in this work were classified into four categories: Ferritic-martenitic steel, austenitic stainless steel, nickel alloys, and special materials. The majority of the work focused on the austenitic stainless steel alloys, followed by three nickel alloys. The alloys investigated in this work are as follows:

Ferritic-martensitic Stainless Steels

- HCM12A

Austenitic Stainless Steels

- F91
- 316SS
- 310SS
- AL-6XN
- 800H

Nickel Alloys

- Haynes 230
- Alloy 625
- PE-16

Special Materials

- PM2000

The characterization of each alloy for this work was broken into photo documentation, surface SEM analyses, weight gain, and sub-surface oxide analyses. The surface characterization with the SEM revealed important characteristics for several alloys. Alloy F91 undergoes substantial weight gain and has very poor oxide characteristics: The oxide is porous, unstable, and readily undergoes spallation. Overall, Alloy F91 is unsuitable for use in S-CO_2 environments. The surface SEM analysis of alloy HCM12A revealed that the oxide layer is readily formed on the areas of higher stress, which was indicated by the oxide preferentially growing on the bands created by the 400 grit sand paper. Alloy HCM12A also was susceptible to a high degree of weight gain and poor oxide characteristics such as porosity and spallation. Alloy PM2000 exhibited stable behavior in the S-CO_2 environment, and this alloy had the lowest weight gain with no surface irregularities. Furthermore, Alloy PM2000 developed a thin, stable oxide layer, but did exhibit minor localized oxide spallation, but this may be prevented with better initial surface preparation.

Only alloys F91 and HCM12A performed poor in the weight gain analysis. The remaining alloys all exhibited desirable weight gain characteristics; namely, a low weight gain rate with no sudden weight oscillations, which could be an indication of breakaway oxidation or oxide spallation.

Alloy 625 performed exceptionally in each category. This alloy exhibited no surface irregularities, minor weight gain, and a thin, stable oxide layer.

4.1.2 Weight Gain

The alloys that exhibited the best weight gain performance were 316SS, 310SS, AL-6XN, 800H, Haynes 230, Alloy 625, PE-16, and PM2000. These alloys formed stable, protective films and exhibited no localized corrosion. Furthermore, these alloys exhibited small cumulative weight gain, which was on the order of $4x10^{-5}$ mg/cm^2 after 3000 hours exposure. Alloys HCM12A and F91 fared poorly in the S-CO_2 environment and are recommended to be discontinued from further testing. Both of these alloys exhibited weight gain approximately two orders of magnitude higher than the remaining

eight alloys. The weight gain followed parabolic weight gain behavior, but the overall weight gain is too high for further consideration. The cumulative 3000 hour weight gain for all the alloys is presented in Table 4-1 and Figure 4.1.

Table 4-1: 3000 hr weight gain

Alloy	**Weight gain at 3000 hours** (mg/cm^2)
F91	$4.1x10^{-3}$
HCM12A	$5.5x10^{-3}$
PM2000	$2.1x10^{-5}$
316SS	$8.7x10^{-5}$
310SS	$4.6x10^{-5}$
AL-6XN	$5.2x10^{-5}$
800H	$3.9x10^{-5}$
Haynes 230	$4.4x10^{-5}$
Alloy 625	$2.9x10^{-5}$
PE-16	$4.1x10^{-5}$

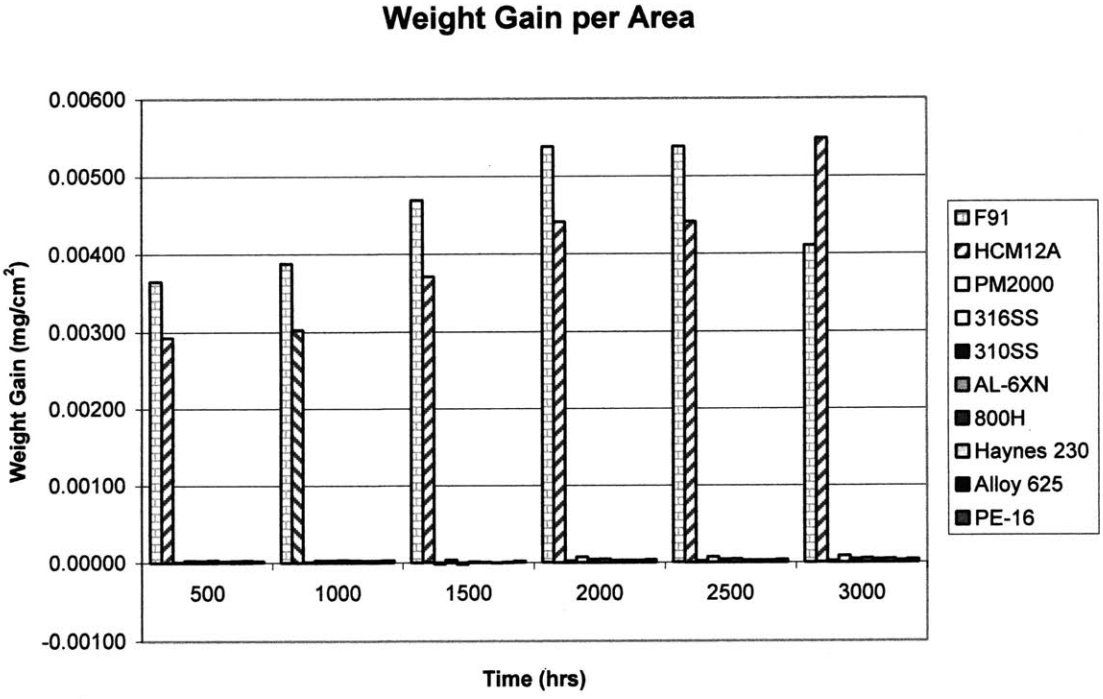

Figure 4.1: Cumulative Weight Gain Per Area

4.1.3 Oxide Growth and Behavior

The oxide growth on alloys HCM12A and F91 was rapid and ultimately ended in oxide spallation. This behavior was first identified in the photo documentation for Alloy F91 and then later in the cross sectional analysis for Alloy HCM12A. The degree of oxide spallation in Alloy F91 is severe and flaked off in large pieces, as evident in the dark and light spots in Figure 4.2.

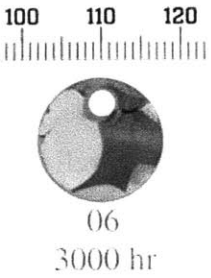

Figure 4.2: Alloy F91 Spallation

The structure of the oxide layers for Alloy HCM12A and F91 was porous and formed as a duplex oxide layer. The outer layer is most likely wustite and the inner layer is a spinel. The oxide in Alloy F91 exhibited the most unstable behavior out of all of the alloys tested, followed by Alloy HCM12A. Alloy F91 exhibited the highest degree of agglomeration of microcracks and is readily detaching from the base metal, as evident in Figure 4.3. Alloy HCM12A exhibited a lesser degree of microcracking, but cracks are still prevalent in the oxide layer. Alloy HCM12A also exhibited a higher degree of porosity than Alloy F91. Lastly, the oxide in Alloy HCM12A can be seen detaching from the base layer, but more locally and not in large flakes. The structure of these two alloys can be seen in Figure 4.3. Both Alloy F91 and HCM12A exhibited a duplex oxide structure with the outer layer iron rich and chromium deficient, while the inner layer contains both iron and chromium. It has not been confirmed that the duplex layer is both wustite and spinel, but it is well documented that wustite is the stable phase about 570°C. This could be confirmed in future work with XPS; however, because these two alloys are recommended for no further scoping work these test are unnecessary.

The high chromium content (>20%), combined with the nickel-base, enables this alloy to develop high oxidation resistance. This is clearly illustrated in Figure 4.4.

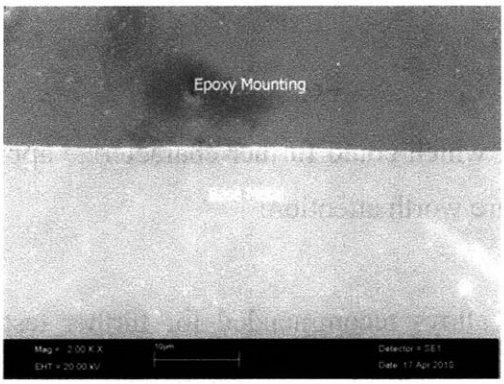

Figure 4.4: Alloy 625

The alloys recommended for future characterization and testing include:

- 316SS
- 316L
- 310SS
- AL-6XN
- 800H
- Haynes 230
- Alloy 625
- PE-16
- PM2000

The alloys recommended for disqualification from the S-CO_2 environment applications are:

- Alloy HCM12A
- Alloy F91

Lastly, it needs to be noted that although Alloy PM2000 performed adequately in this work it was primarily an academic exercise. Alloy PM2000 is an oxide dispersed steel and faces future applicability challenges, such as cost, material processing, and

The high chromium content (>20%), combined with the nickel-base, enables this alloy to develop high oxidation resistance. This is clearly illustrated in Figure 4.4.

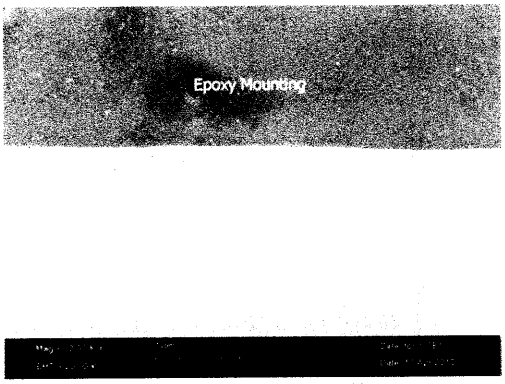

Figure 4.4: Alloy 625

The alloys recommended for future characterization and testing include:

- 316SS
- 316L
- 310SS
- AL-6XN
- 800H
- Haynes 230
- Alloy 625
- PE-16
- PM2000

The alloys recommended for disqualification from the S-CO_2 environment applications are:

- Alloy HCM12A
- Alloy F91

Lastly, it needs to be noted that although Alloy PM2000 performed adequately in this work it was primarily an academic exercise. Alloy PM2000 is an oxide dispersed steel and faces future applicability challenges, such as cost, material processing, and

fabrication such as welding. It is unlikely that this alloy will be deployed in any engineering fashion until these issues are resolved.

4.2 Future Work:

In terms of future testing which could further characterize appropriate alloys covered in this work, the following are worth attention:

- Temperature: the alloys recommended for further testing should be subject to wider temperature windows. The Ellingham Diagram predicts a aluminum oxidation reaction about 850°C. This reaction will be important for those alloys alloyed with aluminum, namely Alloy 800H, 625, PE16, and PM2000. However, this test may be of lower priority because aluminum is a minor constituent in each of these alloys. The high temperature testing is especially important as it includes off normal operating conditions, such as power excursions.
- Extend the pressure envelope to provide additional data to further classify the effect of pressure on oxidation and weight gain. Currently, the pressure envelope has included 12 and 20 MPa. It is important to extend the pressure range from 6 to 30 MPa with adequate intervals to notice small pressure effects.
- Evaluate the cross section of the oxide layer of each alloy at each at shorter time points. The oxides were measured in this work at the 3000 hour time point, but by evaluating the thickness at each time interval the growth, in terms of thickness, can be documented and ultimately developed into an oxidation model.
- Characterization of each oxide layer should include x-ray electron spectroscopy to determine the oxide present.
- Test the most promising alloys in a segregated manner. The current test method tests all of the alloys together. This only provides a qualitative weight gain analysis. There is no way to determine how much of the weight gain is due to trace elements and the distributed among the other alloys. It is unlikely that each sample will have equal affinity for trace elements, dissociated carbon, and dissolved oxygen.

- Further testing should eventually include testing the most likely material candidates under a state of stress. It is important to subject each alloy to the most realistic environment, which includes oxidation under load to determine if applied stress affects the stable passive protection. Currently, all of the testing to date has been only focused on the corrosion behavior of unstressed ingots. It would be helpful to determine the oxide distribution in a stress/strain field to investigate the potential of any abnormal growth/reduction.
- Exposure times in S-CO_2 should extend much further than 3000 hours. This shorter testing window is fine for an initial scoping study to disqualify samples early on, but longer testing is essential. The testing window should extend at least 10,000 hours to understand longer exposure oxidation characteristics.

Extend the testing envelopes, together in pressure, temperature and time will provide additional data to form correlations between temperature, pressure, composition, etc. The temperature testing should include a range from 500-800°C. High temperature and pressure testing (>700°C, >20MPa) becomes challenging as it makes the use of standard high-pressure autoclaves problematic and may require special fabrication. Segregated alloy testing would be wise for only the most promising alloys as it is extremely time consuming and it ties up the testing facilities.

Lastly, it was not specifically outlined here, but it is essential that additional alloys are tested and characterized in S-CO_2. The recent work by Dunlevy, et. al., showed that many nickel alloys are promising for use in the S-CO_2 environments. Future work should include those nickel alloys in a wider evaluation window.

Most importantly, expanding the testing variables requires a much more comprehensive collaboration effort to characterize each alloy. For example, a 10,000 hour test is longer than 1 year and provides only minimal data points for developing correlations and understanding the oxidation characteristics. Longer testing times, extended temperature and pressure ranges, and possible segregated testing places a large burden on each facility and points to the need for multiple, collaborative facilities.

Appendix

This appendix contains the SEM micrographs, photo documentation, and elemental maps of the major constituents for the following alloys: Haynes 230, AL-6XN, PE-16, 316SS, and 800H.

Alloy Haynes 230

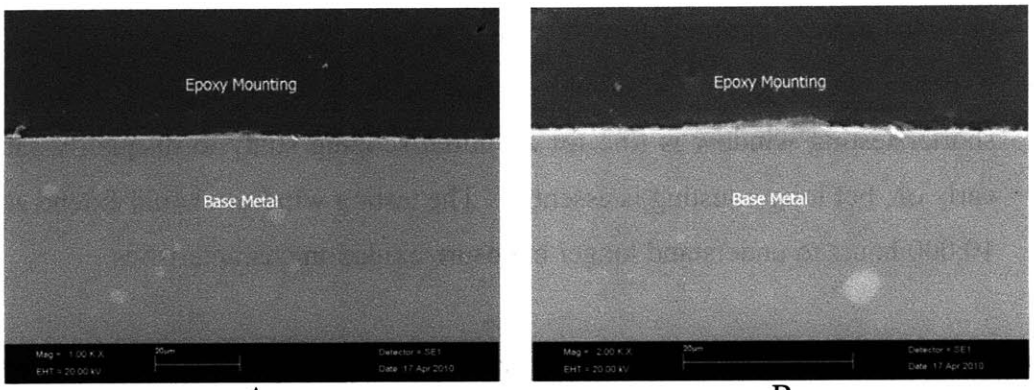

A B

C

Figure A.1: SEM micrographs and photo documentation of Alloy Haynes 230

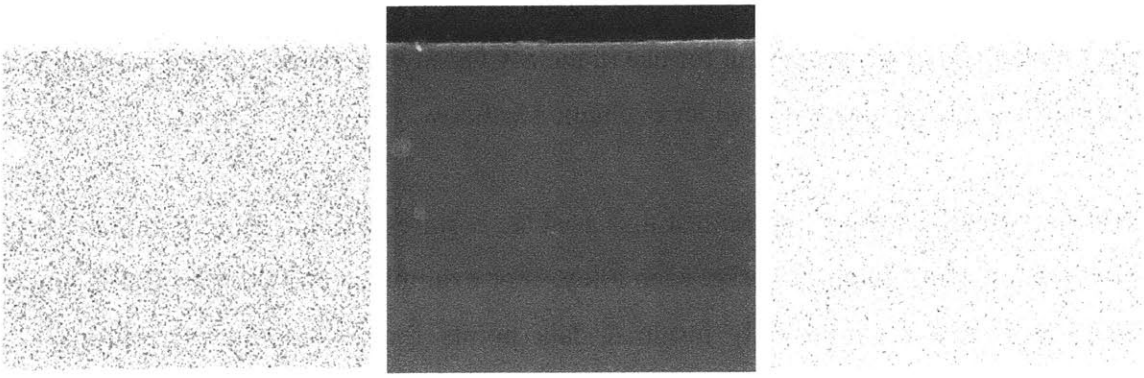

Nickel EDX Map Alloy at 1000X Chromium EDX Map

Figure A.2: Elemental maps for major constituents in Alloy Haynes 230

Alloy AL-6XN

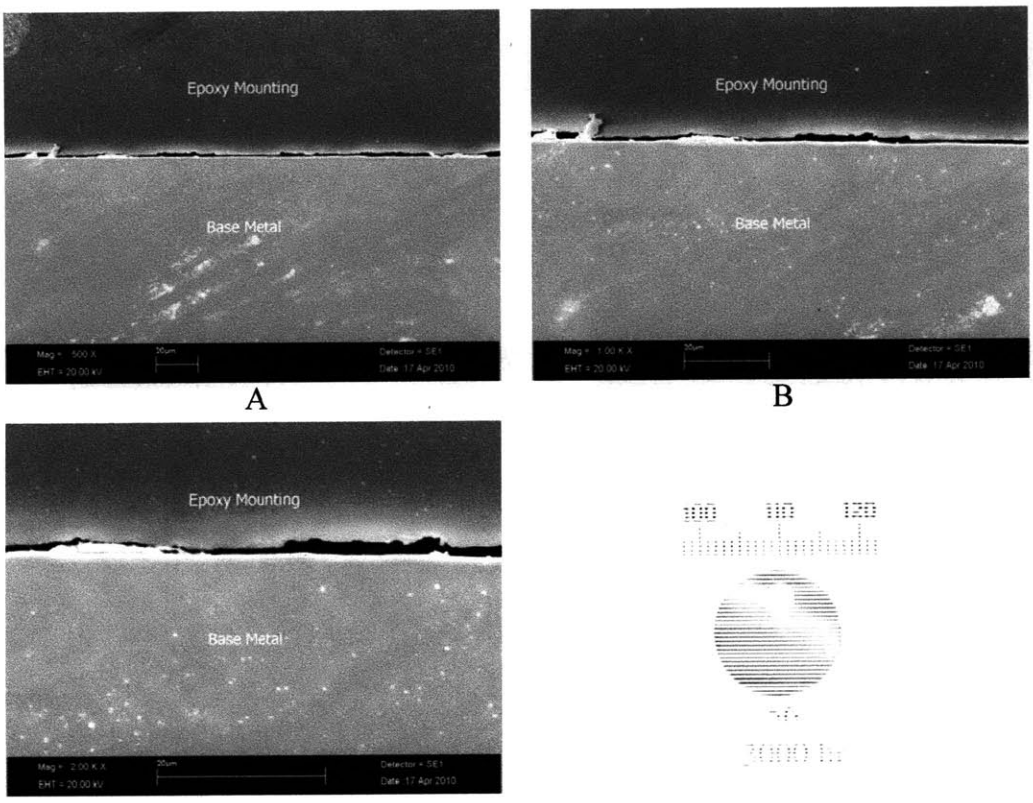

Figure A.3 - SEM Micrographs[2] and photo documentation[3] of Alloy AL-6XN

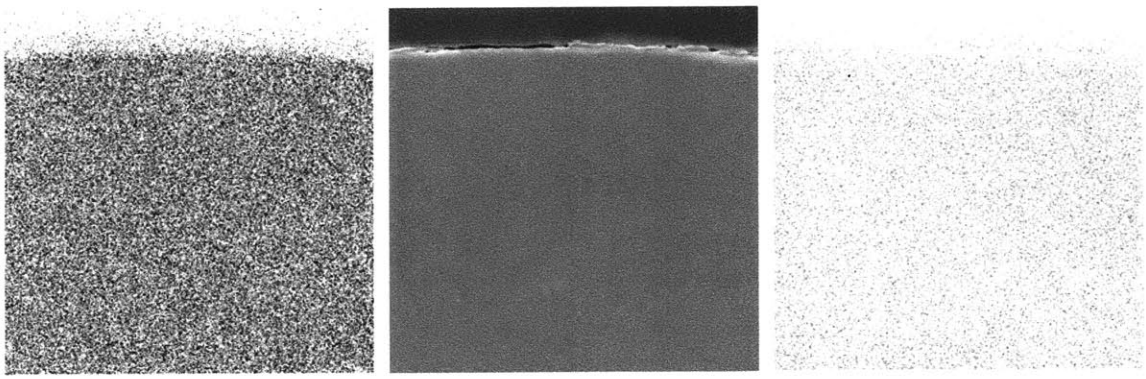

Iron EDX Map | Alloy at 1000X | Chromium EDX Map

Figure A.4 Figure A. 4- Elemental maps for major constituents in Alloy AL-6XN

[2] Light colored particulate in SEM micrographs are alumina oxide, which were used in the final polishing step and are not part of the microstructure

[3] Dimensions on scale for Figure A.3D are in millimeters

Alloy PE-16

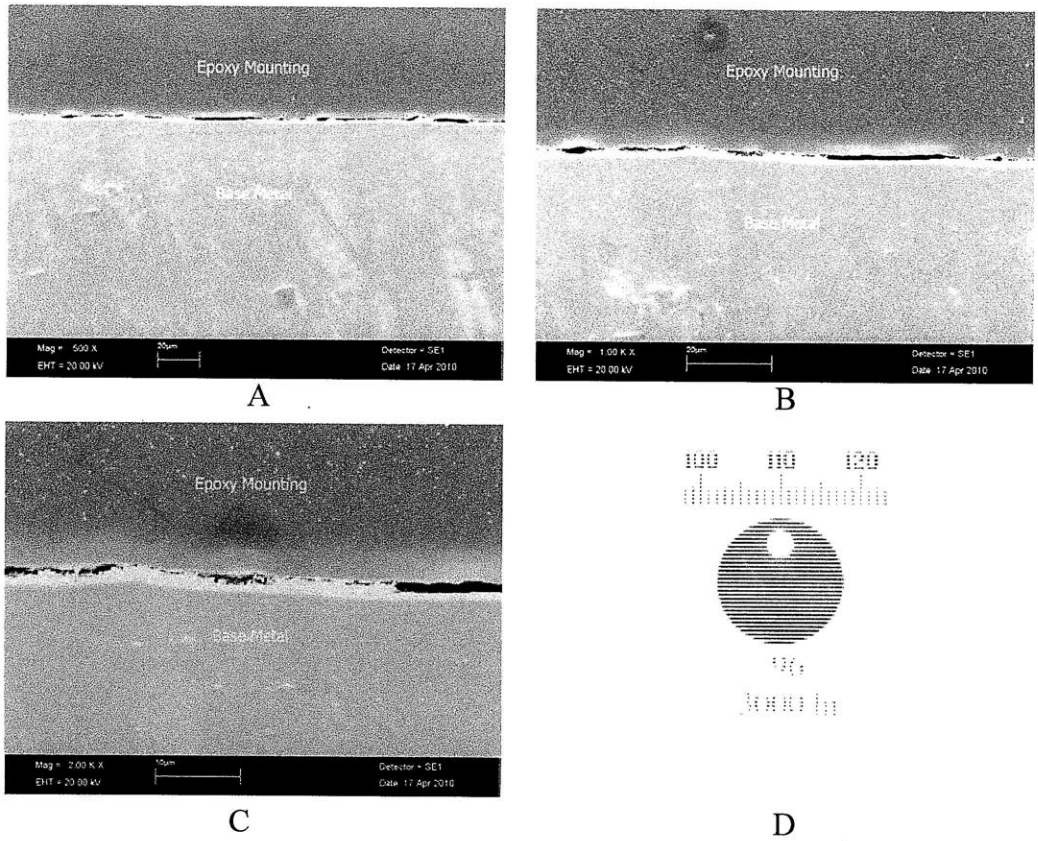

A B C D

Figure A.5 - SEM micrographs and photo documentation[4] of Alloy PE-16

[4] Dimensions on scale for Figure A.5D are in millimeters

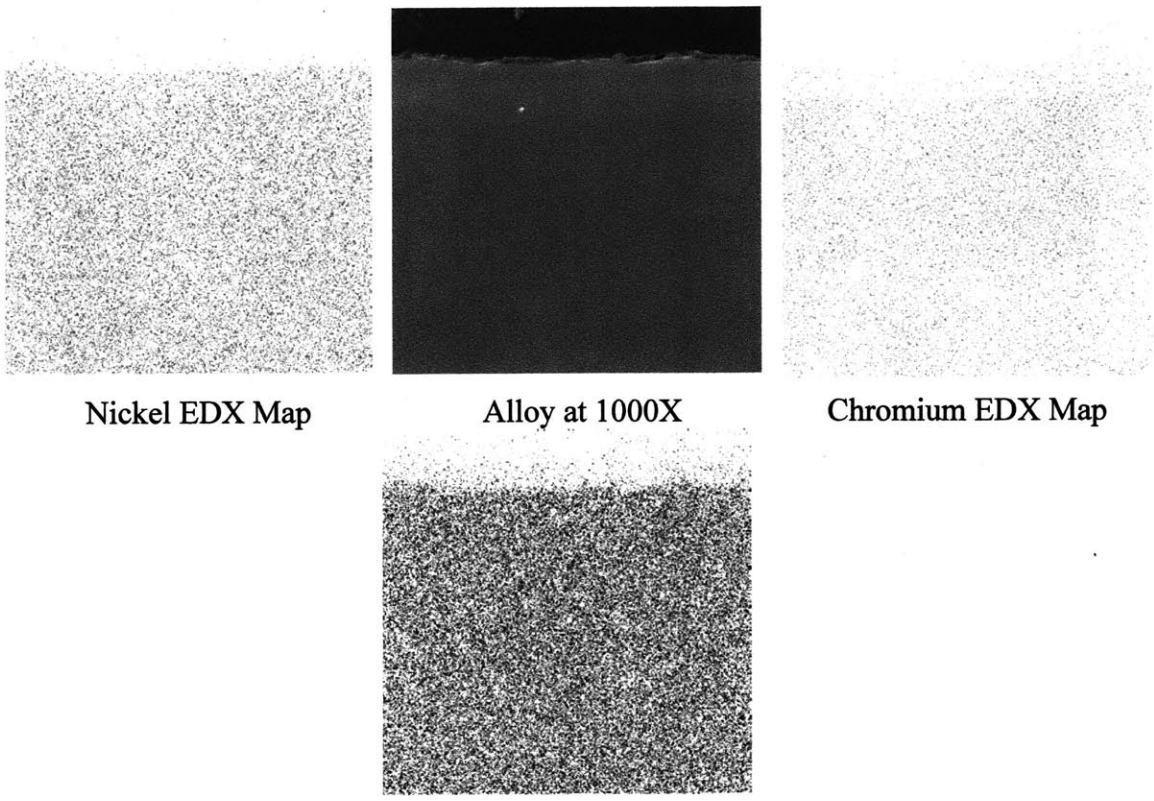

Figure A.6 - Figure A. 6 - Elemental maps for major constituents in Alloy PE-16

Alloy 316SS

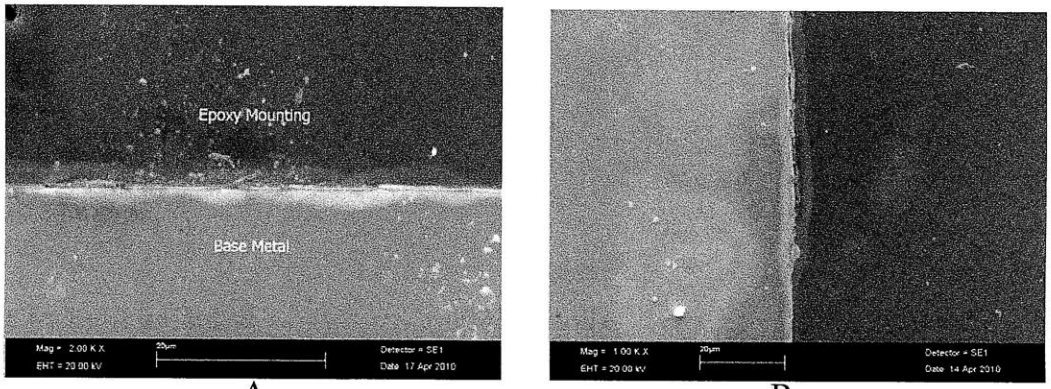

Figure A.7 - SEM micrographs[5] and photo documentation[6] of Alloy 316SS

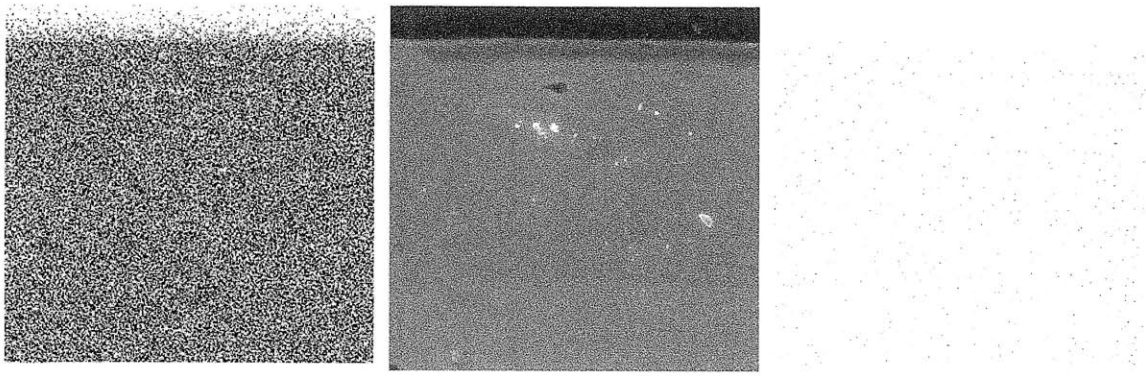

Iron EDX Map Alloy at 1000X Chromium EDX Map

Figure A.8 - Elemental maps for major constituents in Alloy 316SS

[5] Light colored particulate in SEM micrographs are alumina oxide, which were used in the final polishing step and are not part of the microstructure

[6] Dimensions on scale for Figure A.7C are in millimeters

Alloy 800H

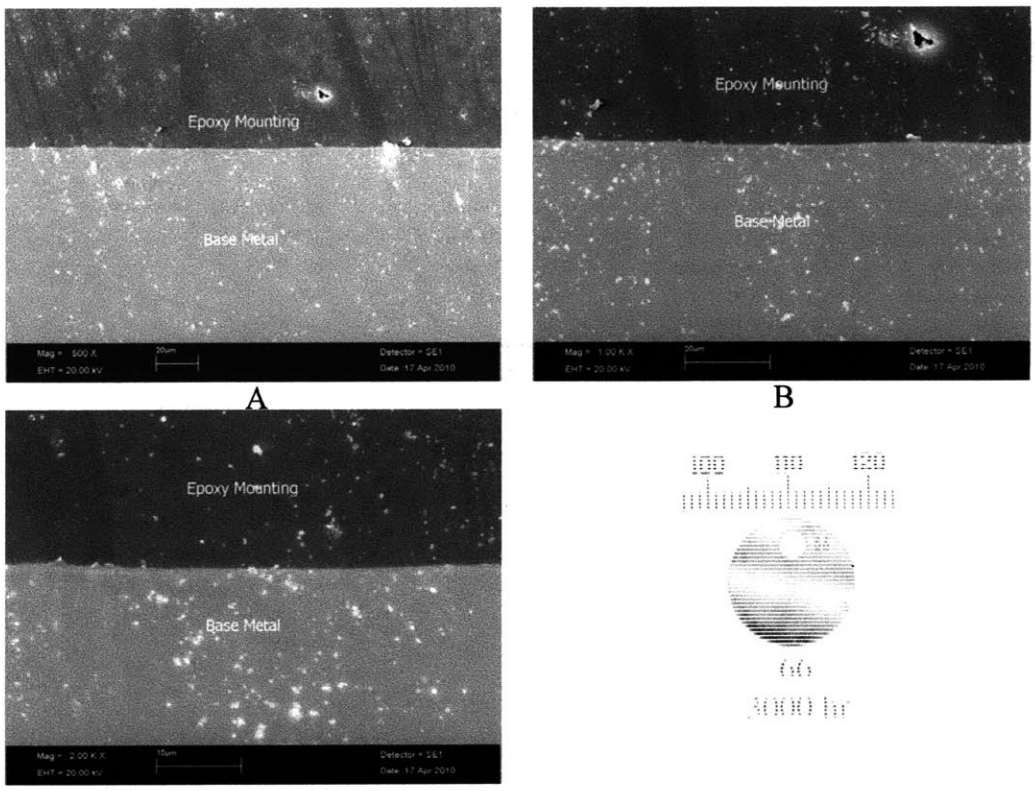

Figure A.9 - SEM micrographs[7] and photo documentation[8] of Alloy 800H

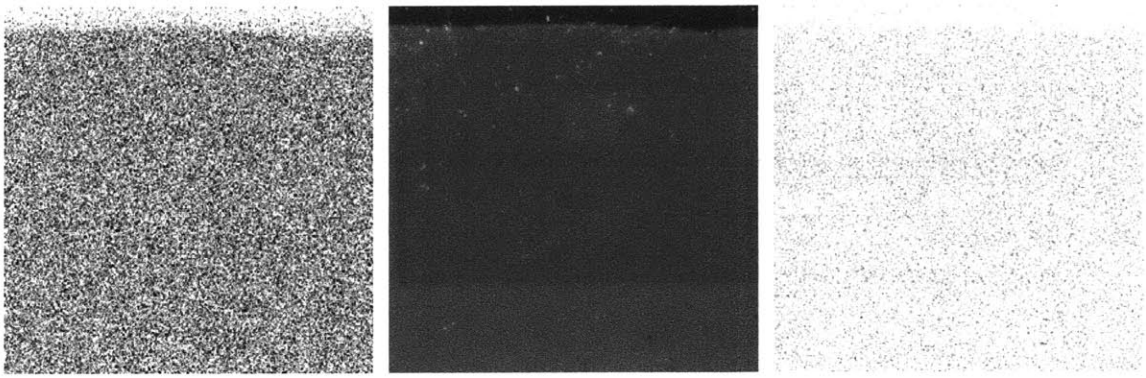

Iron EDX Map Alloy at 1000X Chromium EDX Map

Figure A.10 - Elemental maps for major constituents in Alloy 800H

[7] Light colored particulate in SEM micrographs are alumina oxide, which were used in the final polishing step and are not part of the microstructure

[8] Dimensions on scale for Figure A.9D are in millimeters

CO_2 Certificate of Analysis

Airgas

CERTIFICATE OF ANALYSIS

CARBON DIOXIDE - SFC/SFE

Airgas Specialty Gases
600 Union Landing Road
Riverton, NJ 08077
(856) 829-7878
Fax (856) 829-0571
www.airgas.com

Part Number:	CD SFX15A	Reference Number:	82-124130182-1
Cylinder Analyzed:	XC032972B	Cylinder Volume:	35 Pounds
Laboratory:	ASG - Riverton - NJ	Cylinder Pressure:	835 PSIG
Analysis Date:	Mar 07, 2008	Valve Outlet:	320
Lot #:	82-124130182-1		

ANALYTICAL RESULTS

Component	Requested Purity	Certified Concentration
CO2SFE/SFC	99.9999%	99.9999%
TOTAL CONDENSABLE HYDROCARBONS	< 10 PPB	< 10 PPB
TOTAL HALOCARBONS	< 1 PPB	< 1 PPB
MOISTURE	< 250 PPB	< 250 PPB

Notes:

Impurities verified against analytical standards traceable to NIST by weight and/or analysis.

QA Approval

Page 1 of 82-124130182-1

#5000